



HAL
open science

Dynamics of a stratified vortex under the complete Coriolis force: two-dimensional three-components evolution

Iman Toghraei, Paul Billant

► **To cite this version:**

Iman Toghraei, Paul Billant. Dynamics of a stratified vortex under the complete Coriolis force: two-dimensional three-components evolution. *Journal of Fluid Mechanics*, 2022, 950, pp.A29. 10.1017/jfm.2022.812 . hal-03844881

HAL Id: hal-03844881

<https://hal.science/hal-03844881>

Submitted on 9 Nov 2022

HAL is a multi-disciplinary open access archive for the deposit and dissemination of scientific research documents, whether they are published or not. The documents may come from teaching and research institutions in France or abroad, or from public or private research centers.

L'archive ouverte pluridisciplinaire **HAL**, est destinée au dépôt et à la diffusion de documents scientifiques de niveau recherche, publiés ou non, émanant des établissements d'enseignement et de recherche français ou étrangers, des laboratoires publics ou privés.

Banner appropriate to article type will appear here in typeset article

1 Dynamics of a stratified vortex under the complete 2 Coriolis force: two-dimensional three-components 3 evolution

4 Iman Toghraei¹†, and Paul Billant¹

5 ¹LadHyX, CNRS, École polytechnique, Institut Polytechnique de Paris, 91120 Palaiseau, France

6 (Received xx; revised xx; accepted xx)

7 We study the dynamics of an initially axisymmetric and vertical Lamb-Oseen vortex in a
8 stratified-rotating fluid under the complete Coriolis force on the f plane, i.e. in presence of
9 a background rotation both along the vertical and horizontal directions. By a combination
10 of direct numerical simulations and asymptotic analyses for small horizontal background
11 rotation, we show that a critical layer appears at the radius where the angular velocity of the
12 vortex is equal to the buoyancy frequency when the Froude number is larger than unity. This
13 critical layer generates a vertical velocity which is invariant along the vertical and which
14 first increases linearly with time and then saturates at an amplitude scaling like $Re^{1/3}$, where
15 Re is the Reynolds number. In turn, a quasi-axisymmetric anomaly of vertical vorticity is
16 produced at the critical radius through the non-traditional Coriolis force. Below a critical
17 non-traditional Rossby number \widetilde{Ro} (based on the horizontal component of the background
18 rotation) depending on Re , the Rayleigh's inflectional criterion is satisfied and a shear
19 instability is subsequently triggered rendering the vertical vorticity fully non-axisymmetric.
20 The decay of the angular velocity is then enhanced until it is everywhere lower than the
21 buoyancy frequency. A theoretical criterion derived from the Rayleigh condition predicts
22 well the instability. It shows that this phenomenon can occur even for a large non-traditional
23 Rossby number \widetilde{Ro} for large Re . Hence, the non-traditional Coriolis force might have much
24 more impact on geophysical vortices than anticipated by considering the order of magnitude
25 of \widetilde{Ro} .

26 **Key words:** Authors should not enter keywords on the manuscript, as these must be chosen by
27 the author during the online submission process and will then be added during the typesetting
28 process (see [Keyword PDF](#) for the full list). Other classifications will be added at the same
29 time.

30 **MSC Codes** (*Optional*) Please enter your MSC Codes here

† Email address for correspondence: iman.toghraei@ladhyx.polytechnique.fr

Abstract must not spill onto p.2

31 1. Introduction

32 The Coriolis force due to the planetary rotation is an essential ingredient of geophysical
 33 fluid dynamics. When studying its effect on fluid motions, it is common to use the so-called
 34 traditional approximation which amounts to take into account only the vertical component,
 35 $\Omega_b \sin(\phi)$, of the planetary angular velocity vector Ω_b at a given latitude ϕ . Its horizontal
 36 component $\Omega_b \cos(\phi)$ is neglected mainly because the associated Coriolis force (called non-
 37 traditional Coriolis force) involves vertical motions or appears in the vertical momentum
 38 equation, whereas geophysical flows are usually in hydrostatic balance with weak vertical
 39 motions compared to horizontal motions (Gerkema *et al.* 2008).

40 However, Gerkema *et al.* (2008) have reviewed several circumstances where the effect of
 41 the non-traditional Coriolis force becomes non-negligible. This occurs for example when
 42 the vertical velocity is not small like for the instability of Ekman layers (Wippermann
 43 1969; Etling 1971) and for deep convection (Sheremet 2004). In the latter case, its effect is
 44 particularly intuitive since convective cells become slanted along the axis of rotation instead
 45 of the direction of gravity. The non-traditional Coriolis force may have also many effects
 46 on equatorial flows (Hayashi & Itoh 2012; Igel & Biello 2020) and on the propagation and
 47 frequency range of internal waves, especially when the stratification is weak (Gerkema *et al.*
 48 2008). Recently, the non-traditional force has been shown to significantly modify several
 49 instabilities: the inertial instability (Tort *et al.* 2016; Kloosterziel *et al.* 2017), the symmetric
 50 instability (Zeitlin 2018) and the shear instability (Park *et al.* 2021). Tort & Dubos (2014) and
 51 Tort *et al.* (2014) have also derived shallow water models taking into account the complete
 52 Coriolis force.

53 In the case of vortices, Lavrovskii *et al.* (2000) and Semenova & Slezkin (2003) have
 54 shown analytically that the equilibrium shape of a meddy-like anticyclonic vortex in a
 55 stratified fluid is slightly tilted with respect to the horizontal in presence of the full Coriolis
 56 force. However, they have assumed that the vortex has a uniform vorticity and is embedded
 57 within a fluid at rest. Hence, there exist both a discontinuity of vorticity and velocity at the
 58 vortex boundary. Here, we study numerically and theoretically the evolution of a vortex
 59 with a continuous distribution of vorticity under the complete Coriolis force. The vortex is
 60 initially axisymmetric and columnar with a vertical axis in a stratified-rotating fluid under
 61 the Boussinesq and f -plane approximations. Since there is a misalignment between the
 62 buoyancy force and the rotation vector, this configuration is somewhat similar to the tilted
 63 vortex in a stratified non-rotating fluid considered by Boulanger *et al.* (2007, 2008). They
 64 have shown that a critical layer develops at the radius where the angular velocity of the
 65 vortex is equal to the Brunt–Väisälä frequency. Near this critical layer, they observed an
 66 intense axial flow and strong density variations that are uniform along the vortex axis but
 67 that lead to a three-dimensional shear instability under certain circumstances. We will show
 68 that a similar critical layer develops in the present configuration when the Froude number
 69 is larger than unity. For some parameters, an instability will be also triggered but it will be
 70 two-dimensional instead of being three-dimensional and due to a different mechanism. In
 71 addition, we will show that the critical layer evolution contains two different regimes: first, an
 72 unsteady inviscid phase followed by a second viscous phase which can be steady or can evolve
 73 non-linearly depending on the parameters. Such evolution is similar to the one evidenced by
 74 Wang & Balmforth (2020, 2021) in their studies of forced baroclinic critical layers. They
 75 have also reported the subsequent development of a two-dimensional shear instability and
 76 studied its non-linear evolution by means of a reduced model. Our investigations are based on
 77 direct numerical simulations coupled to asymptotic analyses of the critical layer in the limit
 78 of small non-traditional Coriolis parameter following the lines of Boulanger *et al.* (2007,
 79 2008); Wang & Balmforth (2020, 2021).

80 As a preliminary remark, we stress that the present study has been first carried out by
 81 means of three-dimensional numerical simulations. However, the flow turned out to remain
 82 independent of the vertical coordinate although the vertical velocity is non-zero. In other
 83 words, the dynamics were two-dimensional but with 3 components of velocity (2D3C). As
 84 we will see later, this can be easily understood from the governing equations. For this reason,
 85 the subsequent simulations reported in this paper have been restricted to a two-dimensional
 86 configuration. However, in a future paper, we will show that the introduction of infinitely
 87 small three-dimensional perturbations may also lead for some parameters to a full three-
 88 dimensionalisation of the vortex, i.e. a 3D3C dynamics, via an axial shear instability similar
 89 to the one reported by Boulanger *et al.* (2007, 2008). We stress that the two-dimensional
 90 dynamics is still observed in this full three-dimensional configuration in a significant range
 91 of the parameters space.

92 The paper is organized as follows. The problem is first formulated in §2. Direct numerical
 93 simulations are described in §3. Asymptotic analyses are conducted for small non-traditional
 94 Coriolis parameter in §4. In §5, the numerical and asymptotic results are compared. The origin
 95 of the full non-axisymmetric dynamics of the vortex will be investigated in §6. Finally, the
 96 late evolution is discussed in §7 and the conclusions are given in §8.

97 2. Formulation of the problem

98 2.1. Governing equations

99 We use the incompressible Navier-Stokes equations under the Boussinesq approximation

$$100 \quad \nabla \cdot \mathbf{u} = 0, \quad (2.1)$$

$$102 \quad \frac{\partial \mathbf{u}}{\partial t} + (\mathbf{u} \cdot \nabla) \mathbf{u} = -\nabla \left(\frac{p}{\rho_0} \right) + b \mathbf{e}_z - 2\mathbf{\Omega}_b \times \mathbf{u} + \nu \nabla^2 \mathbf{u}, \quad (2.2)$$

$$103 \quad \frac{\partial b}{\partial t} + \mathbf{u} \cdot \nabla b + N^2 u_z = \kappa \nabla^2 b, \quad (2.3)$$

104 where \mathbf{u} is the velocity field, p is the pressure and $b = -g\rho/\rho_0$ is the buoyancy, g is the
 105 gravity, ρ is the density perturbation and ρ_0 is a constant reference density. \mathbf{e}_z is the vertical
 106 unit vector and $\mathbf{\Omega}_b$ is the background rotation vector. It is assumed to have not only a vertical
 107 component but also a horizontal component along the y direction: $2\mathbf{\Omega}_b = \tilde{f} \mathbf{e}_y + f \mathbf{e}_z$ where
 108 $f = 2\Omega_b \sin(\phi)$ and $\tilde{f} = 2\Omega_b \cos(\phi)$, where ϕ is the latitude or, equivalently, the angle
 109 between the background rotation vector and the unit vector in the y direction, \mathbf{e}_y (figure 1).
 110 ν and κ are the viscosity of the fluid and diffusivity of the stratifying agent, respectively. The
 111 total density field ρ_t reads $\rho_t(\mathbf{x}, t) = \rho_0 + \bar{\rho}(z) + \rho(x, t)$, where $\bar{\rho}$ is the mean density profile
 112 along the z -axis. The Brunt–Väisälä frequency

$$113 \quad N = \sqrt{-\frac{g}{\rho_0} \frac{d\bar{\rho}}{dz}} \quad (2.4)$$

114 will be assumed to be constant.

115 2.2. Initial conditions

116 A single vertical vortex with a Lamb-Oseen profile is taken as initial conditions. Its vorticity
 117 field reads

$$118 \quad \boldsymbol{\omega}(\mathbf{x}, t = 0) = \zeta \mathbf{e}_z = \frac{\Gamma}{\pi a_0^2} e^{-r^2/a_0^2} \mathbf{e}_z, \quad (2.5)$$

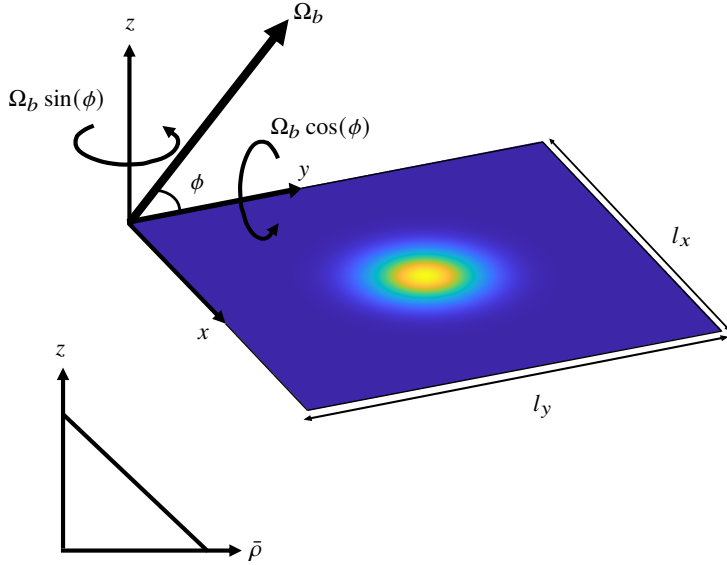


Figure 1: Sketch of the initial vortex in a stratified fluid and in presence of a background rotation Ω_b inclined with an angle ϕ

119 where Γ is the circulation, a_0 is the radius and r is the radial coordinate. The geometry of
 120 the flow is sketched in figure 1.

121 2.3. Non-dimensionalization

122 Equations (2.1-2.3) are non-dimensionalized by using $2\pi a_0^2/\Gamma$ and a_0 as time and length
 123 units:

$$124 \quad \nabla \cdot \mathbf{u} = 0, \quad (2.6)$$

$$125 \quad \frac{\partial \mathbf{u}}{\partial t} + (\mathbf{u} \cdot \nabla) \mathbf{u} = -\nabla p + b \mathbf{e}_z - 2 \left(\frac{1}{Ro} \mathbf{e}_z + \frac{1}{\widetilde{Ro}} \mathbf{e}_y \right) \times \mathbf{u} + \frac{1}{Re} \nabla^2 \mathbf{u}, \quad (2.7)$$

$$126 \quad \frac{\partial b}{\partial t} + \mathbf{u} \cdot \nabla b + \frac{1}{F_h^2} u_z = \frac{1}{ReSc} \nabla^2 b, \quad (2.8)$$

127 where the same notation has been kept for the non-dimensional variables. Note that ρ_0 has
 128 been eliminated by redefining the pressure p . The Reynolds, Froude, Rossby and Schmidt
 129 numbers are defined as
 130

$$131 \quad Re = \frac{\Gamma}{2\pi\nu}, \quad F_h = \frac{\Gamma}{2\pi a_0^2 N}, \quad Ro = \frac{\Gamma}{\pi a_0^2 f}, \quad \widetilde{Ro} = \frac{\Gamma}{\pi a_0^2 \tilde{f}}, \quad Sc = \frac{\nu}{\kappa}. \quad (2.9)$$

132 Note that two Rossby numbers Ro and \widetilde{Ro} are defined based on the two components of the
 133 rotation vector. The Schmidt number will be always set to unity. In the following, all results
 134 will be reported in non-dimensional form.

135

136 2.4. Numerical method

137 A pseudo-spectral method with periodic boundary conditions is used to integrate the
 138 equations (2.1-2.3) in space (Deloncle *et al.* 2008). Time integration is performed with

139 a fourth-order Runge–Kutta scheme. Most of the aliasing is removed by truncating the top
 140 one third of the modes along each direction. The viscous and diffusive terms are integrated
 141 exactly. The horizontal sizes of the computational domain have been set to $l_x = l_y = 18$. As
 142 shown by Bonnici (2018) and Billant & Bonnici (2020), this is sufficiently large to minimize
 143 the effects of the periodic boundary conditions and to give results independent of the box sizes.
 144 In particular, the periodic boundary condition imposes that the net circulation over the domain
 145 is zero implying that the initial vorticity is not exactly (2.5) but $\zeta' = \zeta - \Gamma/(l_x l_y)$. However,
 146 with $l_x = l_y = 18$, the artificial background vorticity $\Gamma/(l_x l_y)$ is weak and represents only
 147 1% of the maximum vorticity of the vortex. The horizontal resolution has been varied from
 148 $n_x = n_y = 512$ for $Re = 2000$ up to $n_x = n_y = 1024$ for $Re = 10000$. As mentioned in the
 149 introduction, preliminary simulations were fully three-dimensional with a resolution n_z and
 150 a vertical size l_z similar to the horizontal ones. However, the flow were always observed to
 151 remain independent of the vertical coordinate. It can be seen indeed from (2.6–2.8) that if
 152 $\partial/\partial z = 0$ at $t = 0$, then the flow will remain independent of the vertical coordinate for all
 153 time. Therefore, only two-dimensional simulations but with 3 components of velocity will
 154 be presented in the following. Several tests using different horizontal resolutions have been
 155 performed in order to verify the accuracy of the computations. For $Re = 2000$, the velocity
 156 has been found to differ by less than 0.1% when the resolution is increased from 512×512
 157 to 1024×1024 . Similarly, for $Re = 10000$, the relative variation of the velocity is less than
 158 0.5% when the resolution is increased from 1024×1024 to 1536×1536 .

159 3. Direct Numerical Simulations

160 3.1. Illustrative example of the vortex dynamic

161 To get an overview of the effect of the complete Coriolis force, we start by presenting the
 162 vortex evolution for the sample set of parameters $Re = 2000$, $F_h = 10$, $Ro = 23.1$, $\phi = 60^\circ$
 163 ($\widetilde{Ro} = 40$). Figures 2 and 3 show the evolution of the vertical velocity and vertical vorticity at
 164 six different times (A movie is available in the supplementary material). Initially, the vortex
 165 is completely axisymmetric (figure 3(a)) and the vertical velocity is zero (figure 2(a)).
 166 As time goes on, a vertical velocity field with an azimuthal wavenumber $m = 1$ develops
 167 (figure 2(b)). This structure tends to intensify and becomes more and more concentrated at
 168 a particular radius (figure 2(c)). Concomitantly, a ring of negative vertical vorticity appears
 169 and grows at the same radius (figure 3(b, c)). Later, the vertical velocity structure and the
 170 ring of anomalous vertical vorticity are no longer perfectly circular (figure 3(d, e, f)). Two
 171 negative vortices appear on the vertical vorticity ring and revolve around the vortex center
 172 (figure 3(e, f)). Simultaneously, the shape of the vertical velocity structure is deformed
 173 similarly (figure 2(e, f)). As already mentioned, preliminary three-dimensional simulations
 174 with various vertical sizes l_z of the computational domain and resolutions n_z have shown
 175 that the velocity and vorticity fields remain always completely independent of the vertical
 176 coordinate, i.e. the same evolution is observed in any horizontal cross-section. It is also
 177 important to stress that this phenomenon occurs only in presence of the complete Coriolis
 178 force. Indeed, if $\widetilde{Ro} = \infty$, the vertical velocity remains identically zero while the vertical
 179 vorticity simply decays by viscous diffusion.

180 From figure 3, we can distinguish two phases in the evolution of the vortex. First, a circular
 181 ring of anomalous vertical vorticity develops and then, this ring becomes non-axisymmetric.
 182 A more in-depth analysis of these two phases will be discussed later. Let us first examine the
 183 effects of the control parameters on this phenomenon.

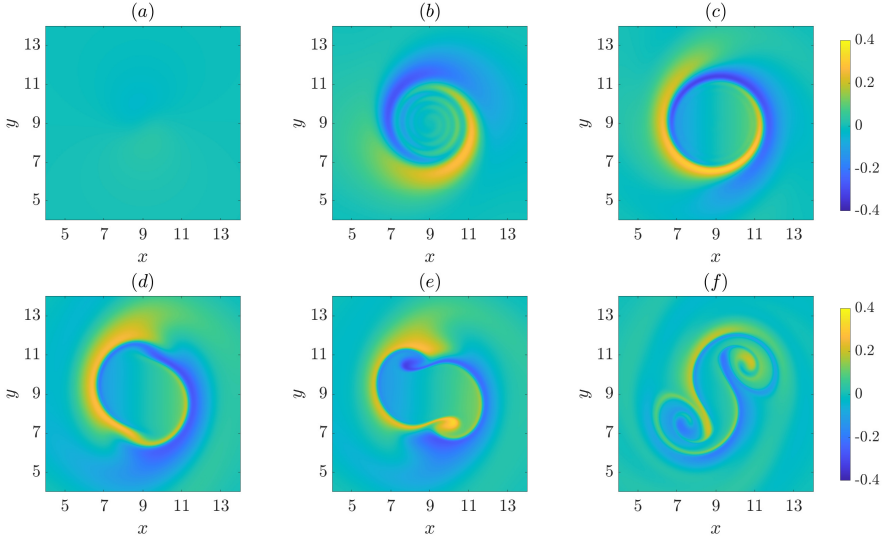


Figure 2: Vertical velocity at different times: (a) $t = 1$, (b) $t = 30$, (c) $t = 60$, (d) $t = 75$, (e) $t = 80$ and (f) $t = 90$ for $Re = 2000$, $F_h = 10$, $Ro = 23.1$, $\phi = 60^\circ$ ($\widetilde{Ro} = 40$).

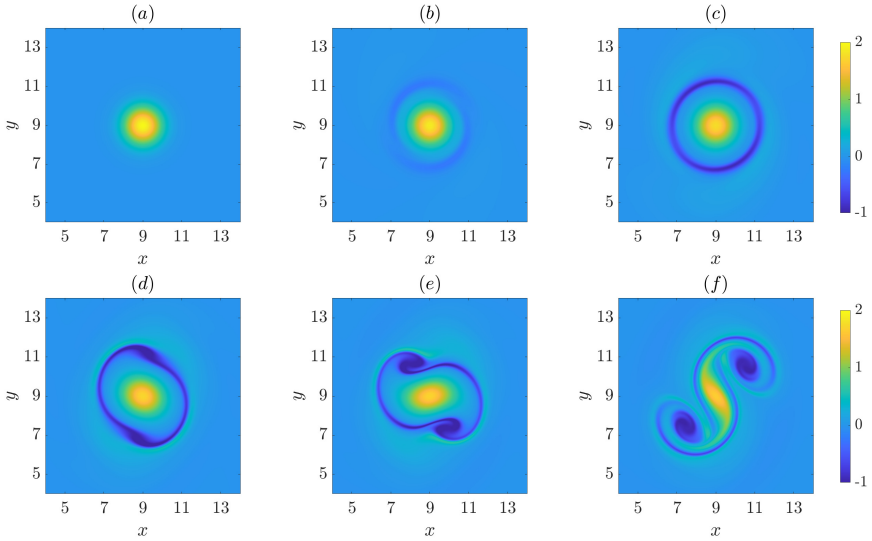


Figure 3: Vertical vorticity at different times: (a) $t = 1$, (b) $t = 30$, (c) $t = 60$, (d) $t = 75$, (e) $t = 80$ and (f) $t = 90$ for $Re = 2000$, $F_h = 10$, $Ro = 23.1$, $\phi = 60^\circ$ ($\widetilde{Ro} = 40$).

184

3.2. Effects of the stratification

185 When the Froude number is decreased from $F_h = 10$ to $F_h = 2$, the same evolution of
 186 the vertical velocity (figure 4 (a) – (d), see the movie in the supplementary material) and
 187 the vertical vorticity (figure 4 (e) – (h)) is observed but at a smaller radius. However, the
 188 anomaly of the vertical vorticity does not become negative this time and the maximum vertical
 189 velocity is also lower than for $F_h = 10$. Figure 5(a) shows the evolution of the vertical velocity

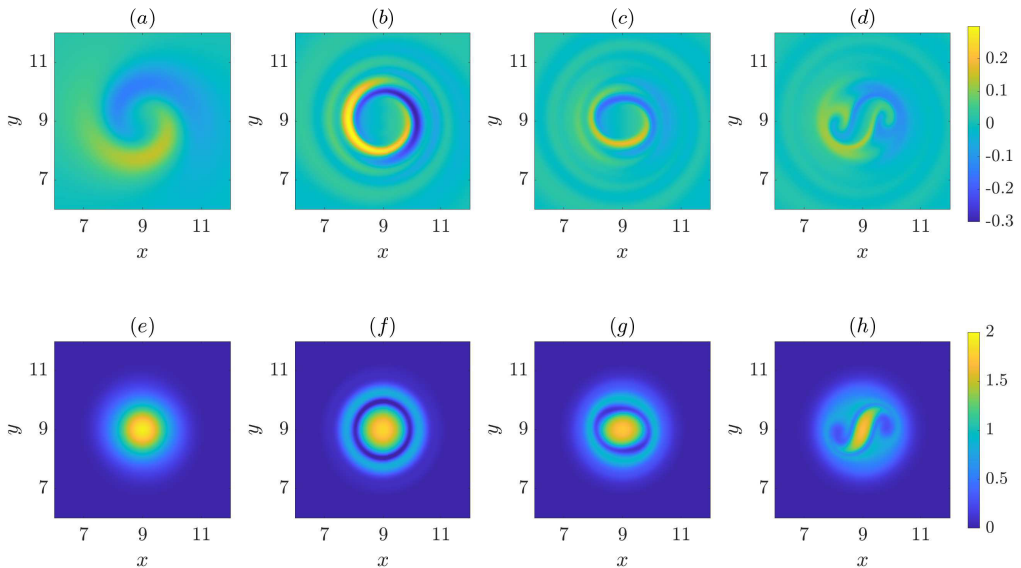


Figure 4: Vertical velocity (top) and vertical vorticity (bottom) at different times: (a, e) $t = 10$, (b, f) $t = 40$, (c, g) $t = 65$ and (d, h) $t = 80$ for $Re = 2000$, $F_h = 2$, $Ro = 23.1$, $\phi = 60^\circ$ ($\widetilde{Ro} = 40$).

190 maximum u_{zm} . In fact, three phases can be distinguished. First, u_{zm} increases linearly with
 191 time with some small oscillations superimposed which will be later attributed to inertia-
 192 gravity waves. The propagation of waves can be also seen in the vertical velocity field at the
 193 beginning of the movies. Then, u_{zm} saturates and tends to slightly decrease. When $t \gtrsim 60$,
 194 large oscillations arise when the vortex becomes fully non-axisymmetric.

195 If the Froude number is below unity, such evolution is no longer observed. In §4, it will be
 196 shown that this phenomenon is due the presence of a critical layer where the angular velocity
 197 of the vortex is equal to the non-dimensional Brunt–Väisälä frequency, i.e. $\Omega = 1/F_h$, where
 198 Ω is the non-dimensional angular velocity of the vortex corresponding to the vorticity field
 199 (2.5).

200

3.3. Effects of the Rossby numbers

201 When the traditional Rossby number Ro , which is based on the vertical component of the
 202 background rotation, is varied, while keeping the other numbers fixed (Re , F_h , \widetilde{Ro}), the
 203 vortex evolution remains strictly identical. This is consistent with the fact that the dynamics
 204 is independent of the vertical coordinate so that the Coriolis force associated with Ro can be
 205 eliminated from (2.7) by redefining the pressure.

206 In contrast, varying the non-traditional Rossby number \widetilde{Ro} , which is based on the horizontal
 207 component of the background rotation, has important effects on the evolution of the vortex.
 208 Since the Rossby number Ro has no effect, the effect of \widetilde{Ro} has been studied by varying the
 209 latitude ϕ while keeping the background rotation rate Ω_b constant. Hence, both \widetilde{Ro} and Ro
 210 varies. Figure 6 shows the evolution of the vertical velocity and vertical vorticity when the
 211 latitude is increased from $\phi = 60^\circ$ to $\phi = 80^\circ$ (\widetilde{Ro} is increased from $\widetilde{Ro} = 40$ to $\widetilde{Ro} = 115.2$)
 212 while keeping the other parameters fixed (A movie is available in the supplementary material).

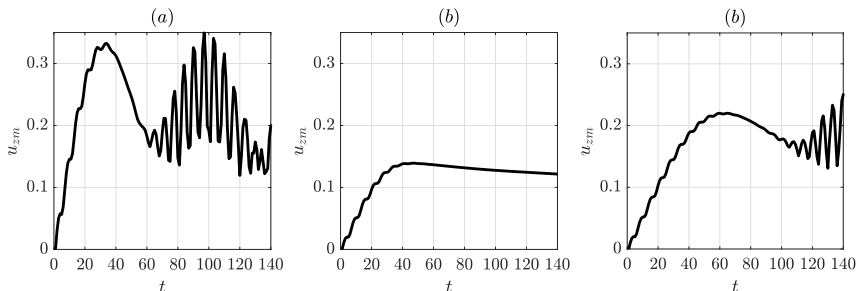


Figure 5: Maximum vertical velocity as a function of time for $F_h = 2$ and (a) $Re = 2000$, $Ro = 23.1$, $\phi = 60^\circ$ ($\widetilde{Ro} = 40$), (b) $Re = 2000$, $Ro = 20.3$, $\phi = 80^\circ$ ($\widetilde{Ro} = 115.2$) and (c) $Re = 10000$, $Ro = 20.3$, $\phi = 80^\circ$ ($\widetilde{Ro} = 115.2$).

213 The initial evolution (figure 6(a, b, e, f)) is similar to the one in figure 4 but, later (figure
 214 6(c, d, g, h)), the fields keep the same shape, i.e. no significant asymmetric deformations can
 215 be seen in contrast to figure 4(d, h). As seen in figure 5(b), only two phases are then present
 216 in the evolution of the maximum vertical velocity. First, a phase where u_{zm} grows linearly
 217 with weak oscillations and, second, a phase where u_{zm} remains approximately constant. In
 218 addition, the maximum vertical velocity is lower (figure 6(b, c)) and the anomalous vorticity
 219 ring is weaker (figure 6(g)) than in figure 4. At late time $t = 200$ (figure 6(d, h)), we can
 220 see that the vertical velocity has decreased by viscous diffusion while the vertical velocity
 221 field has moved towards the center of the vortex. This is consistent with the critical layer's
 222 interpretation since, as the angular velocity decays, the radius where $\Omega = 1/F_h$ decreases.

223

3.4. Effects of the Reynolds number

224 Figure 7 shows the evolution of the vertical velocity and vertical vorticity when the Reynolds
 225 number is increased from $Re = 2000$ to $Re = 10000$ while keeping the other parameters as
 226 in figure 6. A movie is also available in the supplementary material. The maximum vertical
 227 velocity is almost doubled and the vertical velocity field is much thinner and focused near
 228 a given radius (figure 7(b)) than in figure 6. Furthermore, the ring of anomalous vertical
 229 vorticity (figure 7(f)) is more intense. Later, asymmetric deformations of this ring and
 230 of the vertical velocity field are clearly visible (figure 7(c, d, g, h)) in contrast to figure 6.
 231 Oscillations are then visible in the evolution of u_{zm} (figure 5(c)).

232

3.5. Combined effects of \widetilde{Ro} and Re

233 In the previous sections, we have seen that the vertical vorticity becomes fully non-
 234 axisymmetric in a second stage if ϕ is sufficiently lower than 90° , i.e. if \widetilde{Ro} is not too
 235 large (figure 4) or if the Reynolds number is large enough (figure 7), otherwise the vertical
 236 vorticity field remains quasi-axisymmetric (figure 6). Figure 8 summarizes several other
 237 simulations for various \widetilde{Ro} and Reynolds numbers Re keeping the Froude number equal to
 238 $F_h = 2$. Yellow and blue symbols indicate simulations where the vertical vorticity remains
 239 quasi-axisymmetric or becomes non-axisymmetric, respectively. We can see that the critical
 240 Rossby number \widetilde{Ro}_c above which the vortex remains quasi-axisymmetric increases with the
 241 Reynolds number from $\widetilde{Ro}_c \simeq 100$ for $Re = 2000$ to $\widetilde{Ro}_c \simeq 400$ for $Re = 10000$.

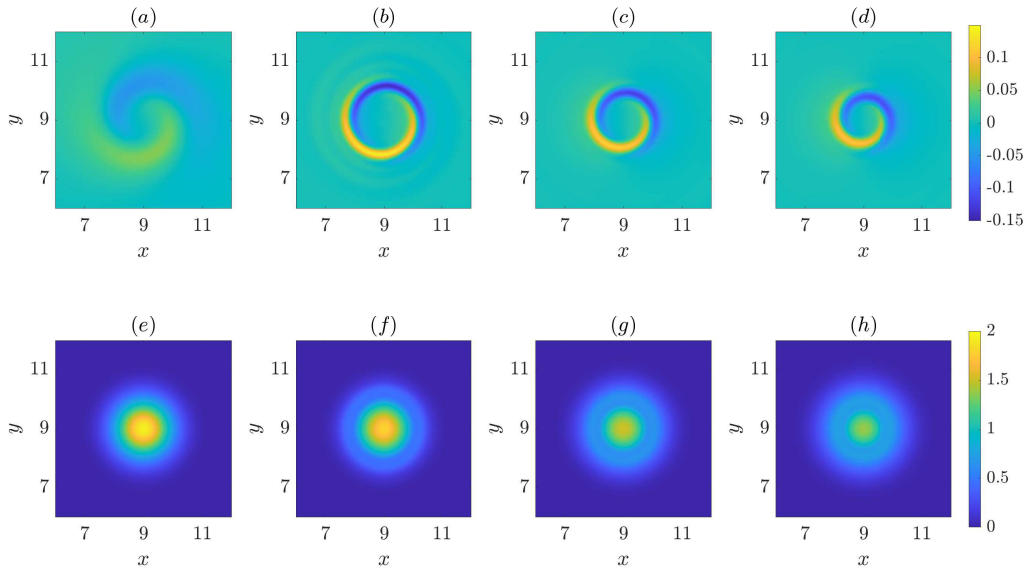


Figure 6: Vertical velocity (top) and vertical vorticity (bottom) at different times: (a, e) $t = 10$, (b, f) $t = 50$, (c, g) $t = 150$ and (d, h) $t = 200$ for $Re = 2000$, $F_h = 2$, $Ro = 20.3$, $\phi = 80^\circ$ ($\widetilde{Ro} = 115.2$).

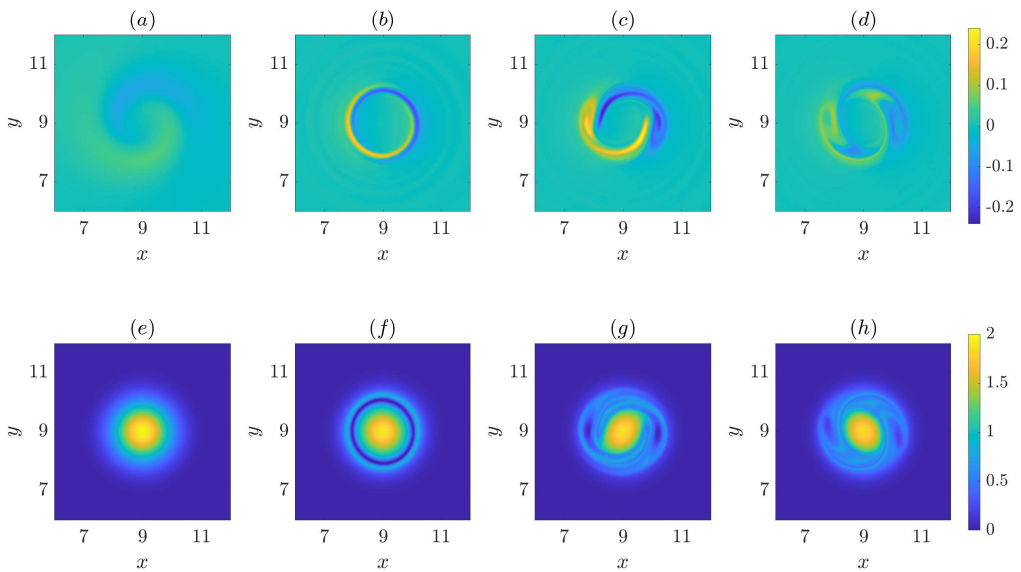


Figure 7: Vertical velocity (top) and vertical vorticity (bottom) at different times: (a, e) $t = 10$, (b, f) $t = 100$, (c, g) $t = 150$ and (d, h) $t = 200$ for $Re = 10000$, $F_h = 2$, $Ro = 20.3$, $\phi = 80^\circ$ ($\widetilde{Ro} = 115.2$).

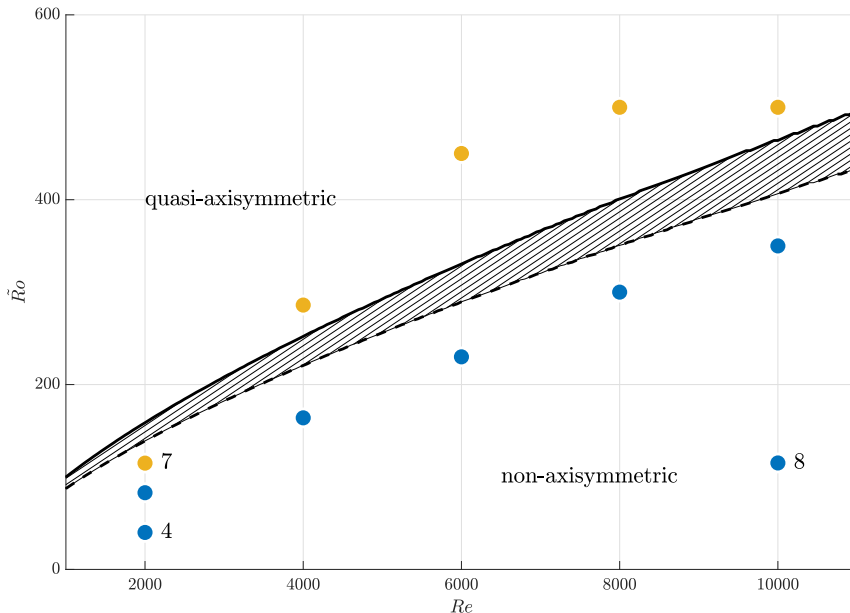


Figure 8: Map of the simulations in the parameter space (Re, \widetilde{Ro}) for $F_h = 2$. The yellow and blue circles represent simulations where the vertical vorticity remains quasi-axisymmetric or not, respectively. The solid and dashed lines represent the criterion (6.14) for different values of (a, c) : $(\infty, 0)$ and $(\infty, 0.4)$, respectively. The number near some points indicate the figure numbers where the corresponding simulation is shown.

242 4. Asymptotic analyses

243 In order to understand the vortex evolution observed in the DNS, it is interesting to perform
 244 an asymptotic analysis for small horizontal component of the background rotation, i.e. for
 245 $\widetilde{Ro} \gg 1$, and for large Reynolds number. To this end, it is first convenient to rewrite (2.6-2.8)
 246 in cylindrical coordinates (r, θ, z)

$$247 \quad \frac{1}{r} \frac{\partial r u_r}{\partial r} + \frac{1}{r} \frac{\partial u_\theta}{\partial \theta} + \frac{\partial u_z}{\partial z} = 0, \quad (4.1a)$$

$$249 \quad \begin{aligned} \frac{\partial u_r}{\partial t} + u_r \frac{\partial u_r}{\partial r} + \frac{u_\theta}{r} \frac{\partial u_r}{\partial \theta} + u_z \frac{\partial u_r}{\partial z} - \frac{u_\theta^2}{r} = -\frac{\partial p}{\partial r} + \frac{2u_\theta}{Ro} - \frac{2u_z}{\widetilde{Ro}} \cos(\theta) \\ + \frac{1}{Re} \left(\nabla^2 u_r - \frac{2}{r^2} \frac{\partial u_\theta}{\partial \theta} \right), \end{aligned} \quad (4.1b)$$

$$251 \quad \begin{aligned} \frac{\partial u_\theta}{\partial t} + u_r \frac{\partial u_\theta}{\partial r} + \frac{u_\theta}{r} \frac{\partial u_\theta}{\partial \theta} + u_z \frac{\partial u_\theta}{\partial z} + \frac{u_r u_\theta}{r} = -\frac{1}{r} \frac{\partial p}{\partial \theta} - \frac{2u_r}{Ro} + \frac{2u_z}{\widetilde{Ro}} \sin(\theta) \\ + \frac{1}{Re} \left(\nabla^2 u_\theta + \frac{2}{r^2} \frac{\partial u_r}{\partial \theta} \right), \end{aligned} \quad (4.1c)$$

$$252 \quad \frac{\partial u_z}{\partial t} + u_r \frac{\partial u_z}{\partial r} + \frac{u_\theta}{r} \frac{\partial u_z}{\partial \theta} + u_z \frac{\partial u_z}{\partial z} = -\frac{\partial p}{\partial z} + b + \frac{2u_r}{\widetilde{Ro}} \cos(\theta) - \frac{2u_\theta}{Ro} \sin(\theta) + \frac{1}{Re} \nabla^2 u_z, \quad (4.1d)$$

$$253 \quad \frac{\partial b}{\partial t} + u_r \frac{\partial b}{\partial r} + \frac{u_\theta}{r} \frac{\partial b}{\partial \theta} + u_z \frac{\partial b}{\partial z} + \frac{u_z}{F_h^2} = \frac{1}{ReSc} \nabla^2 b. \quad (4.1e)$$

254 It is also convenient to consider the equation for the vertical vorticity ζ :

$$255 \quad \frac{\partial \zeta}{\partial t} + \mathbf{u} \cdot \nabla \zeta = (\boldsymbol{\omega} + \frac{2}{Ro} \mathbf{e}_z) \cdot \nabla u_z + \frac{2}{r\tilde{Ro}} \left[\frac{\partial}{\partial r} (ru_z \sin(\theta)) + \frac{\partial}{\partial \theta} (u_z \cos(\theta)) \right] + \frac{1}{Re} \Delta \zeta, \quad (4.2)$$

256 where $\boldsymbol{\omega} = \nabla \times \mathbf{u}$.

257 The solution is expanded with the small parameter $\varepsilon = 2/\tilde{Ro} \ll 1$ in the form

$$258 \quad (u_r, u_\theta, u_z, p, b) = (0, u_{\theta 0}, 0, p_0, 0) + \varepsilon(u_{r1}, u_{\theta 1}, u_{z1}, p_1, b_1) + \dots, \quad (4.3)$$

259 where $u_{\theta 0} = r\Omega$, with $\Omega = (1 - e^{-r^2})/r^2$, is the non-dimensional angular velocity of the
260 vortex corresponding to the vorticity field (2.5).

261 It is first instructive to consider a steady and non-diffusive flow, i.e. $\partial/\partial t = 0$ and $Re = \infty$.
262 Then, (4.1b) reduces at leading order to the cyclostrophic balance

$$263 \quad -\frac{u_{\theta 0}^2}{r} = -\frac{\partial p_0}{\partial r} + \frac{2u_{\theta 0}}{Ro}, \quad (4.4)$$

264 whereas (4.1a, 4.1c-4.1e) are identically zero at leading order. At first order in ε , it is sufficient
265 to consider only (4.1d) and (4.1e):

$$266 \quad \Omega \frac{\partial u_{z1}}{\partial \theta} = -r\Omega \sin(\theta) + b_1, \quad (4.5a)$$

267

$$268 \quad \Omega \frac{\partial b_1}{\partial \theta} = -\frac{u_{z1}}{F_h^2}. \quad (4.5b)$$

269 The solution is

$$270 \quad u_{z1} = \frac{r\Omega^2 F_h^2}{F_h^2 \Omega^2 - 1} \cos(\theta), \quad (4.6a)$$

271

$$272 \quad b_1 = \frac{-r\Omega}{F_h^2 \Omega^2 - 1} \sin(\theta), \quad (4.6b)$$

273 showing that the Coriolis force due to the horizontal component of the background rotation
274 (first term in the right hand side of (4.5a)) forces a vertical velocity and buoyancy fields.
275 These fields are independent of the vertical coordinate as observed in the DNS. However, we
276 can remark that (4.6a-4.6b) are singular if there exists a radius r_c where $\Omega(r_c) = 1/F_h$. Such
277 critical radius exists wherever $F_h > 1$ since the non-dimensional angular velocity decreases
278 from unity on the vortex axis to zero for $r \rightarrow \infty$.

279 A similar critical layer occurs in the case of a tilted vortex in a stratified fluid (Boulanger
280 *et al.* 2007) and in stratified rotating shear flow (Wang & Balmforth 2020). This singularity
281 can be smoothed if the flow is no longer assumed to be steady or inviscid. Although these
282 two effects can a priori operate simultaneously, the unsteadiness turns out to be, first, the
283 dominant effect while diffusive effects are negligible followed by a second phase where it is
284 the opposite.

4.1. *Unsteady inviscid analysis*

285

286 Accordingly, we first consider (4.1a-4.1e) in the inviscid limit $Re = \infty$ but keeping the time
287 derivatives. At leading order, the equations reduce to

$$288 \quad -\frac{u_{\theta 0}^2}{r} = \frac{\partial p_0}{\partial r} + \frac{2u_{\theta 0}}{Ro}, \quad (4.7)$$

289

$$290 \quad \frac{\partial u_{\theta 0}}{\partial t} = 0, \quad (4.8)$$

291 so that $u_{\theta 0} = r\Omega$ as before. At first order, the equations (4.1d-4.1e) become

$$292 \quad \frac{\partial u_{z1}}{\partial t} + \Omega \frac{\partial u_{z1}}{\partial \theta} = b_1 - r\Omega \sin(\theta), \quad (4.9a)$$

293

$$294 \quad \frac{\partial b_1}{\partial t} + \Omega \frac{\partial b_1}{\partial \theta} = -\frac{u_{z1}}{F_h^2}. \quad (4.9b)$$

295 The only difference with (4.6) is the presence of the time derivatives. By imposing $u_{z1} =$
296 $b_1 = 0$ at $t = 0$, the solutions can be found in the form

$$297 \quad u_{z1} = u_{zp} e^{i\theta} + u_{zp}^* e^{-i\theta}, \quad (4.10a)$$

298

$$299 \quad b_1 = b_p e^{i\theta} + b_p^* e^{-i\theta}, \quad (4.10b)$$

300 where the star denotes the complex conjugate and

$$301 \quad u_{zp} = \frac{r\Omega}{4} \left[-\frac{1}{\alpha} (1 - e^{i\alpha t}) + \frac{1}{\beta} (1 - e^{-i\beta t}) \right], \quad (4.11a)$$

302

$$303 \quad b_p = -i \frac{r\Omega}{4F_h} \left[\frac{1}{\alpha} (1 - e^{i\alpha t}) + \frac{1}{\beta} (1 - e^{-i\beta t}) \right], \quad (4.11b)$$

304 with

$$305 \quad \alpha = \frac{1 - F_h \Omega}{F_h}, \quad \beta = \frac{1 + F_h \Omega}{F_h}. \quad (4.12)$$

306 Compared to the steady solution (4.6), the additional terms present in (4.11) correspond
307 to waves generated at $t = 0$ to satisfy the initial conditions. These waves oscillate at the
308 frequencies $1/F_h - \Omega$ and $-1/F_h - \Omega$, i.e. the non-dimensional Brunt-Väisälä frequency
309 with an additional Doppler shift coming from the azimuthal motion of the vortex. Hence,
310 they correspond to inertia-gravity waves with zero vertical wavenumber. In contrast to (4.6),
311 we see now that the vertical velocity and buoyancy (4.10a-4.10b) are no longer singular at
312 the radius r_c where $\Omega(r_c) = 1/F_h$. Indeed, we have $(1 - e^{i\alpha t})/\alpha \simeq -it$ when $\alpha \rightarrow 0$ so that
313 (4.11a-4.11b) remain finite at $r = r_c$.

314 Following Wang & Balmforth (2020), the behaviour of these solutions in the vicinity of
315 the critical radius can be studied more precisely by introducing the variable $\eta = r - r_c$. When
317 $\eta \ll 1$, the vertical velocity approximates to

$$318 \quad u_{z1} = \left[\left(\frac{r_c \Omega_c}{2\eta \Omega'_c} + \frac{\Omega_c}{2\Omega'_c} + \frac{r_c}{2} - \frac{r_c \Omega_c'' \Omega_c}{4\Omega_c'^2} \right) (1 - \cos(\eta \Omega'_c t)) + \frac{r_c}{4} \left(1 - \cos\left(\frac{2}{F_h} t\right) \right) \right] \cos(\theta) \\ - \left[\left(\frac{r_c \Omega_c}{2\eta \Omega'_c} + \frac{\Omega_c}{2\Omega'_c} + \frac{r_c}{2} - \frac{r_c \Omega_c'' \Omega_c}{4\Omega_c'^2} \right) \sin(\eta \Omega'_c t) + \frac{r_c}{4} \sin\left(\frac{2}{F_h} t\right) \right] \sin(\theta) + O(\eta), \quad (4.13)$$

319 where the subscript c indicates a value taken at r_c . The terms involving $\eta\Omega'_c t$ in the sin and
 320 cos functions have not been expanded in (4.13) since this quantity can be large when t is large
 321 even for small η . The approximation (4.13) is therefore uniformly valid whatever t . Taking
 322 into account only the leading order, (4.13) can be simplified and rewritten as

$$324 \quad u_{z1} = \frac{r_c \Omega_c t}{2} \left[\left(\frac{1 - \cos U}{U} \right) \cos(\theta) - \frac{\sin U}{U} \sin(\theta) \right] + O(1), \quad (4.14)$$

325 where $U = \eta\Omega'_c t$. This expression shows that the radial profile of the vertical velocity in
 326 the vicinity of r_c depends only on the self-similar variable U . This implies that the vertical
 327 velocity will be more and more concentrated around r_c as time increases. In addition,
 328 (4.14) shows that the amplitude of u_{z1} will increase linearly with time for a fixed value
 329 of U . In practice, the approximation (4.14) will be accurate only when t is large since the
 330 neglected terms are of order unity. Since $\Omega_c = 1/F_h$, this will occur more and more later
 331 when F_h increases. We emphasize that the inertia-gravity wave oscillating at frequency
 332 $1/F_h + \Omega_c = 2/F_h$ is neglected in (4.14) unlike in (4.13).

333 4.2. Unsteady viscous analysis

334 Here, viscous and diffusive effects are taken into account in addition to the time evolution.
 335 Following Boulanger *et al.* (2007) and Wang & Balmforth (2020, 2021), we assume that
 336 the Reynolds number is large $Re \gg 1$ and consider only the vicinity of the critical radius
 337 by introducing a rescaled radius such that $\tilde{r} = Re^{1/3}(r - r_c)$. We also assume that the
 338 evolution occurs over the slow time $T = Re^{-1/3}t$. Since $Re \gg 1$, the leading order solution
 340 of (4.1a-4.1e) is still $u_{\theta 0} = r\Omega$. At order ε , the equations (4.1d-4.1e) become

$$341 \quad \frac{1}{Re^{1/3}} \frac{\partial u_{z1}}{\partial T} + \left(\Omega_c + \frac{\tilde{r}\Omega'_c}{Re^{1/3}} + O\left(\frac{1}{Re^{2/3}}\right) \right) \frac{\partial u_{z1}}{\partial \theta} = b_1$$

$$- \left(r_c \Omega_c + \frac{\tilde{r}(\Omega_c + r_c \Omega'_c)}{Re^{1/3}} + O\left(\frac{1}{Re^{2/3}}\right) \right) \sin(\theta) + \frac{1}{Re^{1/3}} \frac{\partial^2 u_{z1}}{\partial \tilde{r}^2} + O\left(\frac{1}{Re^{2/3}}\right), \quad (4.15a)$$

$$342 \quad \frac{1}{Re^{1/3}} \frac{\partial b_1}{\partial T} + \left(\Omega_c + \frac{\tilde{r}\Omega'_c}{Re^{1/3}} + O\left(\frac{1}{Re^{2/3}}\right) \right) \frac{\partial b_1}{\partial \theta} = -\frac{u_{z1}}{F_h^2} + \frac{1}{Sc} \left[\frac{1}{Re^{1/3}} \frac{\partial^2 b_1}{\partial \tilde{r}^2} + O\left(\frac{1}{Re^{2/3}}\right) \right]. \quad (4.15b)$$

343 These equations can be solved by expanding u_{z1} and b_1 as follows

$$344 \quad u_{z1} = Re^{1/3} [\tilde{u}_{z1}(\tilde{r}, T)e^{i\theta} + c.c.] + \tilde{u}_{z2}(\tilde{r}, T)e^{i\theta} + c.c. + \dots, \quad (4.16a)$$

$$345 \quad b_1 = Re^{1/3} [\tilde{b}_1(\tilde{r}, T)e^{i\theta} + c.c.] + \tilde{b}_2(\tilde{r}, T)e^{i\theta} + c.c. + \dots \quad (4.16b)$$

347 By substituting (4.16a-4.16b) in (4.15a-4.15b), we get at order $O(Re^{1/3})$

$$348 \quad i\Omega_c \tilde{u}_{z1} = \tilde{b}_1, \quad (4.17a)$$

$$349 \quad i\Omega_c \tilde{b}_1 = -\frac{\tilde{u}_{z1}}{F_h^2}, \quad (4.17b)$$

351 which both yields

$$352 \quad \tilde{b}_1 = i\Omega_c \tilde{u}_{z1}. \quad (4.18)$$

353 The equations at order $O(1)$ are

$$354 \quad \frac{\partial \tilde{u}_{z1}}{\partial T} + i\Omega_c \tilde{u}_{z2} + i\tilde{r}\Omega'_c \tilde{u}_{z1} = \tilde{b}_2 - \frac{r_c \Omega_c}{2i} + \frac{d^2 \tilde{u}_{z1}}{d\tilde{r}^2}, \quad (4.19a)$$

$$355 \quad \frac{\partial \tilde{b}_1}{\partial T} + i\Omega_c \tilde{b}_2 + i\tilde{r}\Omega'_c \tilde{b}_1 = -\frac{1}{F_h^2} \tilde{u}_{z2} + \frac{1}{Sc} \frac{d^2 \tilde{b}_1}{d\tilde{r}^2}. \quad (4.19b)$$

356 By using (4.18), the solvability condition to find \tilde{b}_2 and \tilde{u}_{z2} from (4.19a-4.19b) requires \tilde{u}_{z1}
357 to satisfy

$$358 \quad \frac{\partial \tilde{u}_{z1}}{\partial T} + i\tilde{r}\Omega'_c \tilde{u}_{z1} = \frac{i}{4} r_c \Omega_c + \frac{1}{2} \left(1 + \frac{1}{Sc}\right) \frac{d^2 \tilde{u}_{z1}}{d\tilde{r}^2}. \quad (4.20)$$

359 As shown by Wang & Balmforth (2020, 2021), the solution is

$$360 \quad \tilde{u}_{z1} = iA \frac{1}{\pi} \int_0^{|\Omega'_c|T/\gamma} \exp\left(-\frac{z^3}{3} + i\gamma\tilde{r}z\right) dz, \quad (4.21)$$

361 where

$$362 \quad A = \frac{\pi r_c \Omega_c}{2|2\Omega'_c|^{2/3} \left(1 + \frac{1}{Sc}\right)^{1/3}}, \quad \gamma = \frac{|2\Omega'_c|^{1/3}}{\left(1 + \frac{1}{Sc}\right)^{1/3}}. \quad (4.22)$$

363 When $|\Omega'_c|T/\gamma \gg 1$, the upper bound in the integral can be replaced by infinity so that (4.21)
364 recovers the steady solution (Boullanger *et al.* 2007)

$$365 \quad \tilde{u}_{z1} = iA \text{Hi}(i\gamma\tilde{r}), \quad (4.23)$$

366 where Hi is the Scorer's function (Abramowitz & Stegun 1972). We will see that the time
367 interval where both the unsteadiness and viscous effects are important is short so that (4.23)
368 turns out to be reached quickly after the inviscid regime.

369 4.3. Effect on the vertical vorticity

370 We now turn to the study of the effect of the vertical velocity on the vertical vorticity. Since
371 the flow is invariant along the vertical, the equation for the vertical vorticity (4.2) reduces to

$$372 \quad \frac{\partial \zeta}{\partial t} + \mathbf{u} \cdot \nabla \zeta = \frac{\varepsilon}{r} \left[\frac{\partial}{\partial r} (ru_z \sin(\theta)) + \frac{\partial}{\partial \theta} (u_z \cos(\theta)) \right] + \frac{1}{Re} \Delta_h \zeta. \quad (4.24)$$

373 This equation shows that the vertical velocity generated at order $O(\varepsilon)$ will in turn force a
374 vertical vorticity field at order $O(\varepsilon^2)$. In order to compute this second order horizontal flow,
375 the vertical vorticity and stream function can be expanded as

$$376 \quad \zeta = \zeta_0 + \varepsilon^2 \zeta_2 + \dots, \quad (4.25)$$

$$377 \quad \psi = \psi_0 + \varepsilon^2 \psi_2 + \dots, \quad (4.26)$$

379 where (ζ_0, ψ_0) are the non-dimensional vertical vorticity and stream function of the base
380 flow (2.5) and $\zeta_2 = \Delta_h \psi_2$. The second order vertical vorticity follows

$$381 \quad \frac{\partial \zeta_2}{\partial t} + \Omega \frac{\partial \zeta_2}{\partial \theta} - \frac{1}{r} \frac{\partial \psi_2}{\partial \theta} \frac{\partial \zeta_0}{\partial r} = \frac{1}{r} \left[\frac{\partial}{\partial r} (ru_{z1} \sin(\theta)) + \frac{\partial}{\partial \theta} (u_{z1} \cos(\theta)) \right] + \frac{1}{Re} \Delta_h \zeta_2. \quad (4.27)$$

382 Since the first order vertical velocity u_{z1} has an azimuthal wavenumber $m = 1$, ζ_2 and ψ_2 can
383 be sought in the form

$$384 \quad \zeta_2 = \zeta_{20}(r, t) + [\zeta_{22}(r, t)e^{2i\theta} + c.c.], \quad (4.28)$$

$$385 \quad \psi_2 = \psi_{20}(r, t) + [\psi_{22}(r, t)e^{2i\theta} + c.c.]. \quad (4.29)$$

387 In the following, we will determine only the axisymmetric part ζ_{20} since we will show that
388 the component ζ_{22} grows slower than ζ_{20} .

389 4.3.1. *Inviscid evolution of ζ_{20}*

390 When u_{z1} follows the unsteady inviscid expression (4.10a), the axisymmetric vertical
391 vorticity ζ_{20} is given by

$$392 \quad \frac{\partial \zeta_{20}}{\partial t} = -\frac{i}{2r} \frac{\partial}{\partial r} \left(r(u_{zp}^* - u_{zp}) \right). \quad (4.30)$$

394 By assuming that $\zeta_{20} = 0$ at $t = 0$, the solution reads

$$395 \quad \zeta_{20} = \frac{\zeta_0}{4} \left(\frac{\cos(\alpha t) - 1}{\alpha^2} + \frac{\cos(\beta t) - 1}{\beta^2} \right) \\ + \frac{r\Omega\Omega'}{4} \left[\frac{\alpha t \sin(\alpha t) + 2(\cos(\alpha t) - 1)}{\alpha^3} - \frac{\beta t \sin(\beta t) + 2(\cos(\beta t) - 1)}{\beta^3} \right]. \quad (4.31)$$

396 Considering the vicinity of the critical radius $\eta = r - r_c$, this solution approximates at
397 leading order to

$$398 \quad \zeta_{20} = \frac{r_c \Omega_c}{4\Omega_c'^2 \eta^3} \left[2 \left(1 - \cos(\eta \Omega_c' t) \right) - \eta \Omega_c' t \sin(\eta \Omega_c' t) \right] + O\left(\frac{1}{\eta^2}\right), \quad (4.32)$$

399 where ηt has been considered finite as in (4.13) so that the approximation remains valid even
400 for long time. In terms of the similarity variable U , (4.32) can be rewritten

$$401 \quad \zeta_{20} = \frac{r_c \Omega_c \Omega_c' t^3}{4} \left[\frac{2(1 - \cos U) - U \sin U}{U^3} \right] + O\left(\frac{1}{\eta^2}\right). \quad (4.33)$$

402 This expression shows that ζ_{20} remains finite and even vanishes when $U \rightarrow 0$ but ζ_{20} is more
403 and more concentrated in the vicinity of the critical layer as time increases. Furthermore, its
404 amplitude increases like t^3 at leading order.

405 Using the same approach for ζ_{22} , it can be shown that its amplitude grows like t^2 instead
406 of t^3 . Indeed, the forcing term of ζ_{22} is proportional to t^2 like for ζ_{20} but the left hand side of
407 (4.27) is dominated by the term $2i\Omega_c \zeta_{22}$ instead of $\partial \zeta_{20} / \partial t$ for the axisymmetric component.
408 Thus, ζ_{22} is proportional to t^2 , at least initially. This explains why the vertical vorticity is
409 observed in the DNS to remain quasi-axisymmetric during the first two phases.

410 4.3.2. *Viscous evolution of ζ_{20}*

411 When the vertical velocity is given by the unsteady viscous solution (4.16a) and (4.21), it
412 is possible to also obtain its effect on the second order axisymmetric vertical vorticity ζ_{20} .
413 Expressing first (4.27) in terms of \tilde{r} and T gives at leading order when $Re \gg 1$

$$414 \quad \frac{1}{Re^{1/3}} \frac{\partial \zeta_{20}}{\partial T} = \frac{-i}{2} Re^{2/3} \frac{\partial}{\partial \tilde{r}} (\tilde{u}_{z1}^* - \tilde{u}_{z1}) + O(Re^{1/3}) + \frac{1}{Re^{1/3}} \frac{\partial^2 \zeta_{20}}{\partial \tilde{r}^2} + \dots \quad (4.34)$$

415 As shown by Wang & Balmforth (2021), the exact solution of (4.34) can be found by
416 means of a Fourier transform in \tilde{r} using (4.21). This gives

$$417 \quad \zeta_{20} = -i \frac{ReA}{2\gamma\pi} \int_0^{|\Omega_c'|T} \exp\left(\frac{-q^3}{3\gamma^3} + iq\tilde{r}\right) \left(\frac{1 - \exp(q^3/|\Omega_c'| - q^2T)}{q} \right) dq + c.c. \quad (4.35)$$

418 In appendix, an approximation of (4.35) valid for large time $T \gg 1$ is found in the form

$$419 \quad \zeta_{20} = \zeta_{20}^{(1)} + \zeta_{20}^{(2)}, \quad (4.36)$$

420 where

$$421 \quad \zeta_{20}^{(1)}(\tilde{r}) = Re \frac{A}{2} \int_0^{\tilde{r}} (\text{Hi}^*(i\gamma u) + \text{Hi}(i\gamma u)) du, \quad (4.37a)$$

422

$$423 \quad \zeta_{20}^{(2)}(\tilde{r}, t) = -Re \frac{A}{2\gamma} \text{erf} \left(\frac{\tilde{r}}{\sqrt{4tRe^{-1/3}}} \right). \quad (4.37b)$$

424 This approximation shows that ζ_{20} saturates and tends toward (4.37a) for $tRe^{-1/3} \rightarrow \infty$ for
 425 $\tilde{r} = O(1)$. However, when $|\tilde{r}| \rightarrow \infty$ and $tRe^{-1/3}$ is finite, ζ_{20} vanishes. The approximation
 426 (4.36) will be compared to numerical solutions of (4.34) as well as DNS in section (5.2).

427 To summarize, the axisymmetric vertical vorticity correction at order $O(\varepsilon^2)$, ζ_{20} , follows
 428 two distinct regimes. First, it evolves purely inviscidly and grows like t^3 according to (4.31).
 429 Then, it tends to saturate and follows the approximation (4.36) for large times. This shows
 430 that ζ_{20} saturates toward the steady solution (4.37a) for finite \tilde{r} .

431

4.4. Non-linear analysis of the critical layer

432 The viscous linear analysis of the critical layer in sections 4.2 and 4.3 has shown that
 433 the vertical velocity scales as $u_z = O(\varepsilon Re^{1/3})$. This creates a vorticity correction of the
 434 order $\delta\zeta = O(\varepsilon^2 Re)$ (see (4.25), (4.28), (4.36)-(4.37)). Since $r = r_c + \tilde{r}/Re^{1/3}$ in the
 435 critical layer, the corresponding angular velocity correction $\delta\Omega$ is given at leading order by
 436 $\delta\zeta \simeq r_c Re^{1/3} \partial\delta\Omega/\partial\tilde{r}$ so that $\delta\Omega = O(\varepsilon^2 Re^{2/3})$. In turn, we see that this angular velocity
 437 correction would have the same order as the other terms of order $O(1/Re^{1/3})$ in (4.15) if
 438 $\varepsilon^2 Re^{2/3} = O(1/Re^{1/3})$, i.e. if

$$439 \quad Re = \frac{\widetilde{Re}}{\varepsilon^2}, \quad (4.38)$$

440 where \widetilde{Re} is of order unity. For this distinguished limit, there is therefore a non-linear feedback
 441 of the horizontal flow on the evolutions of the vertical velocity and buoyancy as considered
 442 by Wang & Balmforth (2020, 2021). Using the scaling (4.38), the typical order of magnitudes
 443 of the different variables can be expressed in terms of ε only: $u_z = O(\varepsilon^{1/3})$, $b = O(\varepsilon^{1/3})$,
 444 $\delta\zeta = O(1)$, $\delta\Omega = O(\varepsilon^{2/3})$, $u_r = O(\varepsilon^{4/3})$ and the radius and slow time are $\tilde{r} = \varepsilon^{-2/3}(r - r_c)$
 445 and $T = \varepsilon^{2/3}t$, respectively. We also assume $\partial/\partial z = 0$. Accordingly, we expand the variables
 446 as follows:

$$447 \quad u_z = \varepsilon^{1/3} [\tilde{u}_{z1} e^{i\theta} + c.c.] + \varepsilon [\tilde{u}_{z2} e^{i\theta} + c.c.] + \dots, \quad (4.39a)$$

448

$$449 \quad b = \varepsilon^{1/3} [\tilde{b}_1 e^{i\theta} + c.c.] + \varepsilon [\tilde{b}_2 e^{i\theta} + c.c.] + \dots, \quad (4.39b)$$

450

$$451 \quad \Omega = \Omega_0 + \varepsilon^{2/3} \Omega_1 + \dots, \quad (4.39c)$$

452

$$453 \quad u_r = \varepsilon^{4/3} u_{r1} + \dots, \quad (4.39d)$$

454

$$455 \quad \zeta = \zeta_0 + \zeta_1 + \varepsilon^{2/3} \zeta_2 + \dots, \quad (4.39e)$$

456 where Ω_0 and ζ_0 are the non-dimensional angular velocity and vorticity corresponding to
 457 (2.5). In the vicinity of r_c , they can be expanded as

$$458 \quad \Omega_0 = \Omega_c + \tilde{r} \Omega'_c \varepsilon^{2/3} + \dots, \quad (4.40a)$$

459

$$460 \quad \zeta_0 = \zeta_c + \tilde{r} \zeta'_c \varepsilon^{2/3} + \dots \quad (4.40b)$$

461 Note that there are only components of the form $\exp(\pm i\theta)$ in (4.39a-4.39b) because the flow
 462 is invariant along the vertical and because third harmonics arise only at higher order. Then,

464 (4.1d-4.1e) become at leading order

$$\begin{aligned}
 & \varepsilon \frac{\partial \tilde{u}_{z1}}{\partial T} + \varepsilon u_{r1} \frac{\partial \tilde{u}_{z1}}{\partial \tilde{r}} + i \left(\Omega_c + \Omega'_c \tilde{r} \varepsilon^{2/3} \right) \varepsilon^{1/3} \tilde{u}_{z1} + i \varepsilon \Omega_1 \tilde{u}_{z1} + i \varepsilon \Omega_c \tilde{u}_{z2} \\
 & = \varepsilon^{1/3} \tilde{b}_1 + \varepsilon \tilde{b}_2 - \varepsilon \frac{r_c \Omega_c}{2i} + \frac{\varepsilon}{\overline{Re}} \frac{\partial^2 \tilde{u}_{z1}}{\partial \tilde{r}^2} + O\left(\varepsilon^{5/3}\right),
 \end{aligned} \tag{4.41a}$$

$$\begin{aligned}
 & \varepsilon \frac{\partial \tilde{b}_1}{\partial T} + \varepsilon u_{r1} \frac{\partial \tilde{b}_1}{\partial \tilde{r}} + i \left(\Omega_c + \Omega'_c \tilde{r} \varepsilon^{2/3} \right) \varepsilon^{1/3} \tilde{b}_1 + i \varepsilon \Omega_1 \tilde{b}_1 + i \varepsilon \Omega_c \tilde{b}_2 \\
 & = -\frac{\varepsilon^{1/3}}{F_h^2} \tilde{u}_{z1} - \frac{\varepsilon}{F_h^2} \tilde{u}_{z2} + \frac{\varepsilon}{\overline{ReSc}} \frac{\partial^2 \tilde{b}_1}{\partial \tilde{r}^2} + O\left(\varepsilon^{5/3}\right).
 \end{aligned} \tag{4.41b}$$

470 Similarly, the equation (4.2) for the vorticity becomes

$$\begin{aligned}
 & \varepsilon^{2/3} \frac{\partial \zeta_1}{\partial T} + \left(\Omega_c + \Omega'_c \tilde{r} \varepsilon^{2/3} \right) \frac{\partial \zeta_1}{\partial \theta} + \varepsilon^{2/3} \Omega_1 \frac{\partial \zeta_1}{\partial \theta} + \varepsilon^{2/3} u_{r1} \frac{\partial \zeta_1}{\partial \tilde{r}} + \varepsilon^{2/3} \Omega_c \frac{\partial \zeta_2}{\partial \theta} \\
 & = \varepsilon^{2/3} \frac{\partial}{\partial \tilde{r}} \left(\left(\tilde{u}_{z1} e^{i\theta} + \tilde{u}_{z1}^* e^{-i\theta} \right) \sin(\theta) \right) + \frac{\varepsilon^{2/3}}{\overline{Re}} \frac{\partial^2 \zeta_1}{\partial \tilde{r}^2} + O\left(\varepsilon^{4/3}\right).
 \end{aligned} \tag{4.42}$$

472 At leading order, (4.41-4.42) become

$$\varepsilon^{1/3} i \Omega_c \tilde{u}_{z1} = \varepsilon^{1/3} \tilde{b}_1, \tag{4.43a}$$

$$\varepsilon^{1/3} i \Omega_c \tilde{b}_1 = -\frac{\varepsilon^{1/3}}{F_h^2} \tilde{u}_{z1}, \tag{4.43b}$$

$$\Omega_c \frac{\partial \zeta_1}{\partial \theta} = 0. \tag{4.43c}$$

478 The first two equations are identical to (4.17) and the third one implies $\zeta_1 \equiv \zeta_1(\tilde{r}, T)$ and
479 $u_{r1} = 0$. At the next order, we have

$$\frac{\partial \tilde{u}_{z1}}{\partial T} + i \Omega'_c \tilde{r} \tilde{u}_{z1} + i \Omega_1 \tilde{u}_{z1} + i \Omega_c \tilde{u}_{z2} = \tilde{b}_2 - \frac{r_c \Omega_c}{2i} + \frac{1}{\overline{Re}} \frac{\partial^2 \tilde{u}_{z1}}{\partial \tilde{r}^2}, \tag{4.44a}$$

$$\frac{\partial \tilde{b}_1}{\partial T} + i \Omega'_c \tilde{r} \tilde{b}_1 + i \Omega_1 \tilde{b}_1 + i \Omega_c \tilde{b}_2 = -\frac{\tilde{u}_{z2}}{F_h^2} + \frac{1}{\overline{ReSc}} \frac{\partial^2 \tilde{b}_1}{\partial \tilde{r}^2}, \tag{4.44b}$$

$$\frac{\partial \zeta_1}{\partial T} + \Omega_c \frac{\partial \zeta_2}{\partial \theta} = -\frac{i}{2} \frac{\partial}{\partial \tilde{r}} \left(\tilde{u}_{z1}^* - \tilde{u}_{z1} + \tilde{u}_{z1} e^{2i\theta} - \tilde{u}_{z1}^* e^{-2i\theta} \right) + \frac{1}{\overline{Re}} \frac{\partial^2 \zeta_1}{\partial \tilde{r}^2}. \tag{4.44c}$$

485 Equations (4.44a) and (4.44b) are identical to (4.19) except for the presence of the terms
486 involving Ω_1 . They can be combined to give

$$\frac{\partial \tilde{u}_{z1}}{\partial T} + i \Omega'_c \tilde{r} \tilde{u}_{z1} + i \Omega_1 \tilde{u}_{z1} = \frac{i}{4} r_c \Omega_c + \frac{1}{2\overline{Re}} \left(1 + \frac{1}{Sc} \right) \frac{\partial^2 \tilde{u}_{z1}}{\partial \tilde{r}^2}, \tag{4.45}$$

488 whereas (4.44c) splits into

$$\frac{\partial \zeta_1}{\partial T} = -\frac{i}{2} \frac{\partial}{\partial \tilde{r}} \left(\tilde{u}_{z1}^* - \tilde{u}_{z1} \right) + \frac{1}{\overline{Re}} \frac{\partial^2 \zeta_1}{\partial \tilde{r}^2}, \tag{4.46a}$$

$$\Omega_c \frac{\partial \zeta_2}{\partial \theta} = -\frac{i}{2} \frac{\partial}{\partial \tilde{r}} \left(\tilde{u}_{z1} e^{2i\theta} - \tilde{u}_{z1}^* e^{-2i\theta} \right). \tag{4.46b}$$

492 Since $\zeta_1 = r_c \partial \Omega_1 / \partial \tilde{r}$, the equations (4.45-4.46a) form a closed system of equations. An
 493 equation for Ω_1 can be obtained by integrating (4.46a):

$$494 \quad \frac{\partial \Omega_1}{\partial T} = -\frac{i}{2r_c} (\tilde{u}_{z1}^* - \tilde{u}_{z1}) + \frac{1}{Re} \frac{\partial^2 \Omega_1}{\partial \tilde{r}^2}. \quad (4.47)$$

495 Equation (4.46b) shows that the azimuthal wavenumbers $m = \pm 2$ are generated in the
 496 vorticity only at higher order explaining again why the vorticity remains quasi-axisymmetric
 497 in the DNS during the first two phases. For this reason, components of the form $\exp(\pm 3i\theta)$
 498 arise in the vertical velocity and density (4.39a-4.39b) only at the higher order $\varepsilon^{5/3}$.

499 5. Comparison between the DNS and the asymptotic analyses

500 We now compare in details the asymptotic and numerical results.

501 5.1. Vertical velocity

502 Figure 9 shows the evolution of the maximum vertical velocity $u_{zm}(\theta, t)$ (solid line) for
 503 $\theta = 0$ (figure 9(a)) and $\theta = \pi/2$ (figure 9(b)) for the set of parameters $Re = 10000$, $F_h = 2$,
 504 $Ro = 20.3$, $\phi = 80^\circ$ ($\overline{Ro} = 115.2$). Two different angles are considered since the theoretical
 505 vertical velocity has the form $u_z = u_{zc}(r, t) \cos(\theta) + u_{zs}(r, t) \sin(\theta)$. Hence, the plots for
 506 $\theta = 0$ and $\theta = \pi/2$ allow us to check the predictions for u_{zc} and u_{zs} , respectively.

507 We can see that the inviscid theoretical solution (4.10a) (red dashed line in figure 9(a, b))
 508 predicts very well the initial linear increase of the maximum vertical velocity in the DNS
 509 for both angles. The unsteady viscous solution (4.16a, 4.21) (yellow dashed line) increases
 510 also linearly initially and is in good agreement with the DNS except that it lacks the small
 511 oscillations. They are indeed due to inertia-gravity waves oscillating at frequency $1/F_h + \Omega =$
 512 $2/F_h$ near r_c (see the last term of (4.11a)) and of the two lines of (4.13) which are neglected
 513 in (4.14) and section 4.2.

514 When the growth of u_{zm} is no longer linear, the time-dependent viscous solution (4.21)
 515 remains in very good agreement with the DNS and describes perfectly the transition towards
 516 the steady viscous solution (4.23) (green dashed line). The latter solution is close to the
 517 levels of saturation of $u_{zm}(\theta, t)$ for $\theta = 0$ and $\theta = \pi/2$ in the DNS, although the agreement
 518 is not as good as for the initial regime. However, the non-linear equations (4.45, 4.47) (blue
 519 dashed lines) are in better agreement with the DNS indicating that non-linear effects are also
 520 active in the saturation. By essence, none of the theoretical solutions can exhibit oscillations
 521 associated with the late non-axisymmetric evolution observed in the DNS.

522 Figures 9(c, d) show a similar comparison when the Reynolds number is reduced to $Re =$
 523 2000 , keeping the other parameters fixed. In this case, $u_{zm}(\theta = 0, t)$ and $u_{zm}(\theta = \pi/2, t)$ do
 524 not oscillate at late time in the DNS (black solid line). The agreement with (4.10a) and (4.21)
 525 or (4.23) are then excellent in the initial and saturation regimes, respectively. In addition,
 526 we see that the predictions of the non-linear equations (4.45, 4.47) remain very close to the
 527 linear ones, i.e. (4.21), showing that non-linear effects are weak in this case.

528 Figure 9 shows that the transition from the unsteady inviscid solution (4.10a) to the steady
 529 viscous one, (4.23), occurs in a short time range. Therefore, the unsteady viscous solution
 530 (4.21) can be well approximated by (4.10a) for $t \leq \mathcal{T}$ and (4.23) for $t \geq \mathcal{T}$, where

$$531 \quad \mathcal{T} = 2\pi \frac{Re^{1/3} \text{Hi}(0)}{|2\Omega'_c|^{2/3} (1 + 1/Sc)^{1/3}}, \quad (5.1)$$

532 is the time when the overall maximum given by (4.10a) and (4.23) becomes equal. This time

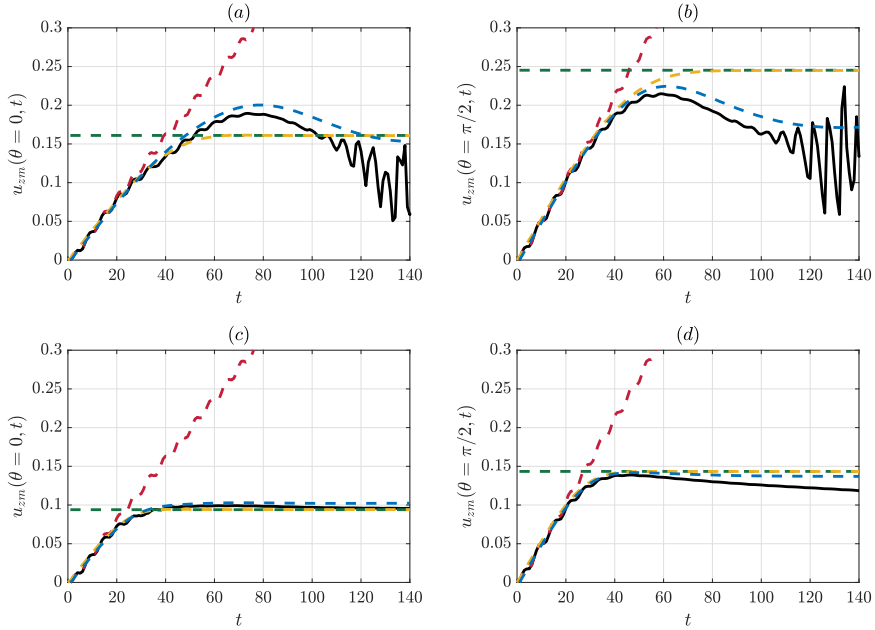


Figure 9: Comparison between the maximum vertical velocity in the DNS (black solid line), predicted by the unsteady inviscid solution (4.10a) (red dashed line), by the unsteady viscous solution (4.16a, 4.21) (yellow dashed line), by the steady viscous solution (4.16a, 4.23) (green dashed line) and by the non-linear equations (4.45, 4.47) (blue dashed line) for (a) $\theta = 0$ and (b) $\theta = \pi/2$ for $Re = 10000$, $F_h = 2$, $Ro = 20.3$, $\phi = 80^\circ$ and for (c) $\theta = 0$ and (d) $\theta = \pi/2$ for $Re = 2000$, $F_h = 2$, $Ro = 20.3$, $\phi = 80^\circ$ ($\widetilde{Ro} = 115.2$).

533 is independent of \widetilde{Ro} and depends only on the Reynolds number, the Froude number via Ω'_c
 534 and the Schmidt number.

535 Figure 10 displays a detailed comparison of the radial profile of u_z for $\theta = 0$ and $\theta = \pi/2$
 536 predicted by (4.10a) (red dashed line) and observed in the DNS (black solid line) for different
 537 instants in the inviscid regime, i.e. $t \leq \mathcal{T}$ for the same parameters as figures 9(a, b). We
 538 see that the agreement is excellent even when $t \simeq \mathcal{T}$ (figures 10(c, f)). The approximation
 539 (4.21) and the solution of the non-linear equations (4.45, 4.47) for the vertical velocity are
 540 also represented by yellow and blue dashed lines, respectively, in figures 10(b, c, e, f). The
 541 approximation (4.14) is almost identical to (4.21) in this time range and not represented.
 542 As expected, the agreement between the DNS and (4.21) or (4.45, 4.47) is very good near
 543 r_c but deteriorates away from r_c . We can notice that the blue and yellow dashed lines are
 544 superposed everywhere except close to the critical radius r_c for $t = 40$ (figures 10(c, f)). In
 545 this region, the blue dashed lines are in very good agreement with the DNS indicating that
 546 non-linear effects are important there. However, away from r_c , it is (4.10a) (red dashed line)
 547 which better agrees with the DNS. For $t = 5$ (figures 10(a, d)), the approximations (4.21)
 548 and (4.45, 4.47) are not accurate and not shown. This is because the profile of u_z is not yet
 549 sufficiently localized around r_c at this early time and, therefore, it cannot be well described
 550 by a local approximation near r_c . Indeed, we can see in figures 10(a, d) that the profiles of
 551 u_z are quite different from those in figures 10(b, c, e, f).

552 Figure 11 shows again the vertical velocity profiles observed in the DNS for the same
 553 parameters, but for $t \geq \mathcal{T}$ this time they are compared to the unsteady and steady viscous

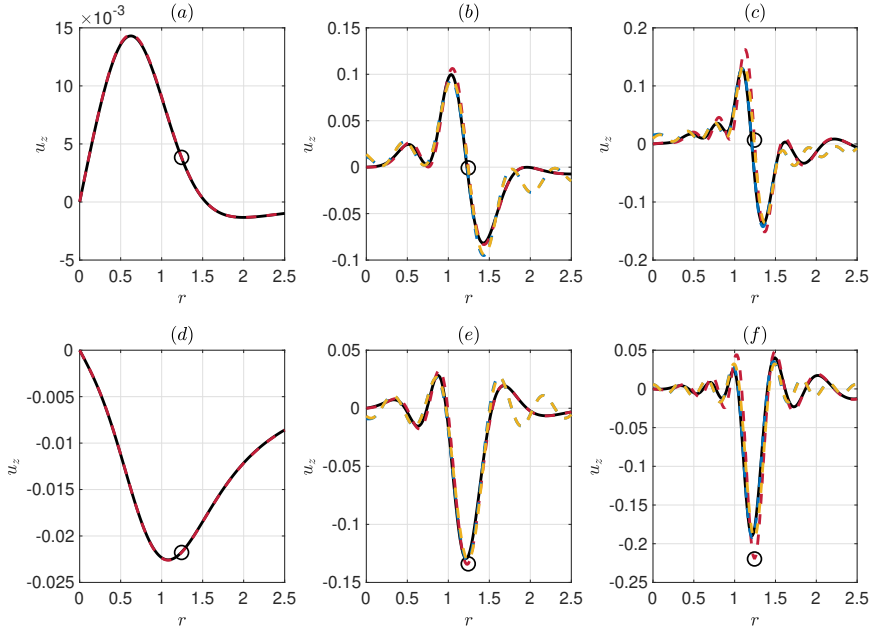


Figure 10: Comparison between the vertical velocity at $\theta = 0$ (top row) and $\theta = \pi/2$ (bottom row) in the DNS (black solid line), predicted by the unsteady inviscid solution (4.10a) (red dashed line), by the unsteady viscous solution (4.21) (yellow dashed line) and by the non-linear equations (4.45,4.47) (blue dashed line) at (a, d) $t = 5$, (b, e) $t = 25$ and (c, f) $t = 40$ for $Re = 10000$, $F_h = 2$, $Ro = 20.3$, $\phi = 80^\circ$ ($\bar{Ro} = 115.2$). The circle symbols represent the location of the critical radius in the unsteady inviscid solution (4.10a).

554 solutions (4.21) (yellow dashed lines) and (4.23) (green dashed lines) as well as the predictions
 555 of the non-linear equations (4.45,4.47) (blue dashed lines). At $t = 40$ (figures 11(a, d)), the
 556 steady viscous solution (4.23) (green dashed lines) is already in good agreement with the DNS
 557 since $t = 40$ is close to the time \mathcal{T} where the transition from (4.10a) to (4.23) occurs (figures
 558 9(a, b)). Nevertheless, it departs slightly from the DNS near r_c unlike the unsteady viscous
 559 solution (4.21) and non-linear predictions from (4.45,4.47). At longer times, $t = 60$ (figures
 560 11(b, e)) and $t = 80$ (figures 11(c, f)), (4.21) and (4.23) become almost identical and remain
 561 in satisfactory agreement with the vertical velocity profiles of the DNS. Nevertheless, we
 562 can see a shift between the numerical and theoretical profiles. In contrast, the solution of the
 563 non-linear equations (4.45,4.47) remains in very good agreement with the DNS and does not
 564 exhibit such shift. This indicates that the shift is due to the viscous and non-linear variations
 565 of the angular velocity. For example, this makes the critical radius where $\Omega(r_c) = 1/F_h$ to
 566 move towards the vortex center as seen in figure 11. This phenomenon is absent from the
 567 linear equations (4.21,4.23) since they do not take into account any variation of the angular
 568 velocity.

569

5.2. Vertical vorticity

570 The asymptotic analyses have shown that the axisymmetric component of the vertical velocity
 571 is given by $\zeta = \zeta_0(r) + \varepsilon^2 \zeta_{20}(r, t) + \dots$, where ζ_{20} follows (4.31) and (4.35) in the inviscid and
 572 viscous regimes, i.e. $t \leq \mathcal{T}$ and $t \geq \mathcal{T}$, respectively. A global view of these two regimes and

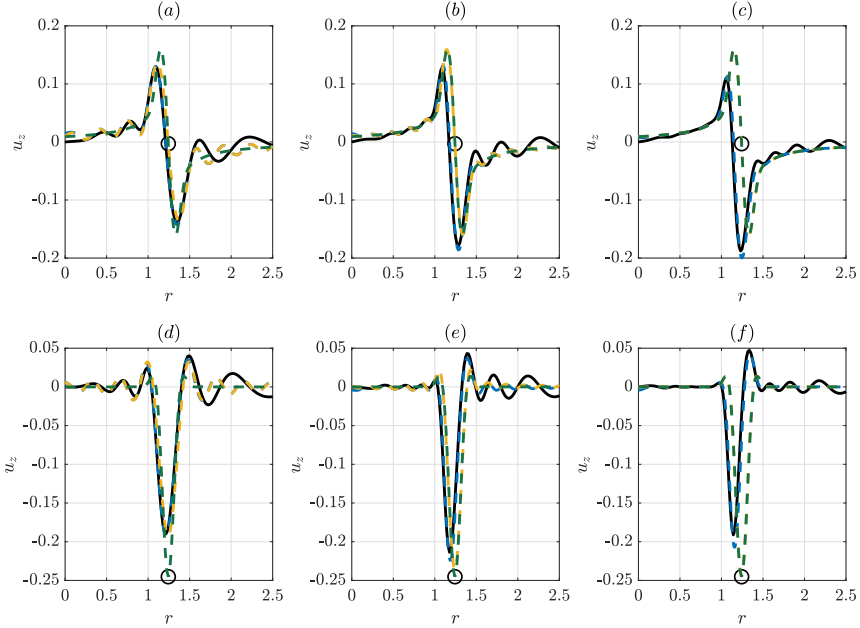


Figure 11: Comparison between the vertical velocity at $\theta = 0$ (top row) and $\theta = \pi/2$ (bottom row) in the DNS (black solid line), predicted by the unsteady viscous solution (4.16a, 4.21) (yellow dashed line), by the steady viscous solution (4.16a, 4.23) (green dashed line) and by the non-linear equations (4.45, 4.47) (blue dashed line) at (a, d) $t = 40$, (b, e) $t = 60$, (c, f) $t = 80$ for $Re = 10000$, $F_h = 2$, $Ro = 20.3$, $\phi = 80^\circ$ ($\widetilde{Ro} = 115.2$). The circle symbols represent the location of the critical radius in the unsteady viscous solution (4.16a).

573 the associated approximations can be gained by plotting $\partial\zeta_{20}/\partial r$ at $r = r_c$ (figure 12). The
 574 black solid line shows the evolution of $\partial\zeta_{20}/\partial r(r_c, t)$ computed numerically from (4.35).
 575 $\partial\zeta_{20}/\partial r(r_c, t)$ increases initially like t^4 in agreement with the approximation (4.33) (red
 576 dashed line). Subsequently, for $t \gg \mathcal{T}$, $\partial\zeta_{20}/\partial r(r_c, t)$ increases more slowly and saturates
 577 towards $\partial\zeta_{20}^{(1)}/\partial r(r_c)$ (black dashed line) for $t \rightarrow \infty$. The approximation (4.36) (blue dashed
 578 line) is in good agreement with the solution (4.35) (black line) in this regime. It will allow
 579 us to derive a theoretical criteria for the onset of non-axisymmetry in section 6.4.

580 Figure 13 compares the radial profile of the theoretical vorticity $\zeta = \zeta_0(r) + \varepsilon^2\zeta_{20}(r, t) + \dots$
 581 with ζ_{20} given by the unsteady inviscid solution (4.31) (red dashed line) to the DNS when
 582 $t \leq \mathcal{T}$. The agreement is excellent and predicts very well the deformation of the vertical
 583 vorticity profile near $r_c \approx 1.2$. A similar comparison is displayed in figure 14 for three
 584 different times such that $t \gtrsim \mathcal{T}$ and ζ_{20} given by the unsteady viscous solution (4.35). The
 585 agreement continues to be very good even for $t = 85$ (figure 14(c)), confirming the validity
 586 of the solution (4.35). A slight shift can be however noticed near r_c and near the vortex axis.
 587 In contrast, the predictions of the non-linear equations (4.45, 4.47) (blue dashed lines) are in
 588 very good agreement with the DNS near r_c . This shows again that non-linear effects are not
 589 negligible in the critical layer.

590 Finally, the prediction for late time $t \gg \mathcal{T}$ based on the steady viscous solution (4.36)
 591 has been compared to a DNS for a larger non-traditional Rossby number $\widetilde{Ro} = 500$, the
 592 other parameters being identical. The vortex remains then quasi-axisymmetric in the DNS

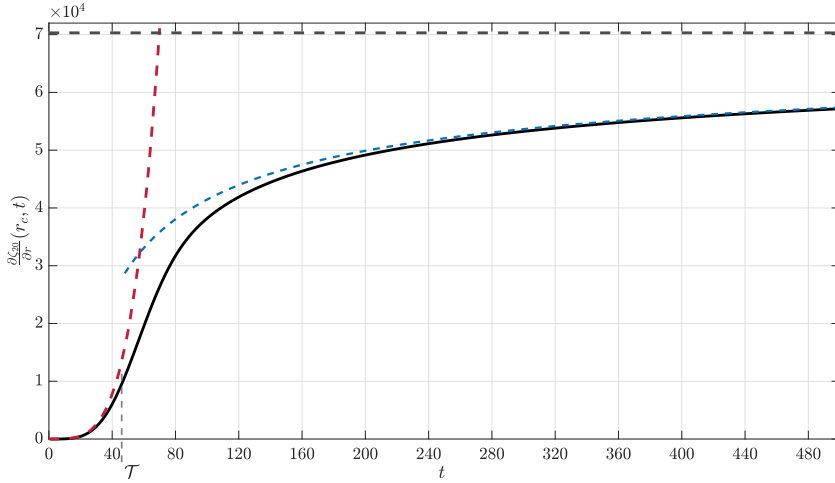


Figure 12: Comparison between the evolution of $\partial\zeta_{20}/\partial r(r_c, t)$ from the theoretical expressions: the unsteady viscous solution (4.35) (Black solid line), the unsteady inviscid solution (4.31) (red dashed line), the viscous solutions (4.36) (blue dashed line) and (4.37a) (black dashed line) for $Re = 10000$, $F_h = 2$.

593 (figure 8) allowing us to see the late evolution of the vorticity without the non-axisymmetric
 594 perturbations. Figure 15 shows that the deformation of the vorticity profile near r_c is weak
 595 but well predicted by (4.36) although there is a shift for $t \geq 300$. In this case, the predictions
 596 from the non-linear equations (4.45, 4.47) (not shown) are identical to those from (4.36)
 597 indicating that the non-linear effects are weak. However, if we take also into account the
 598 global viscous decay of the leading order vorticity ζ_0 which is significant for these large
 599 times, then the agreement with the DNS is perfect (yellow dashed line)

600 Besides, a feature of high interest is that the vertical vorticity profile exhibits two extrema
 601 near r_c , $d\zeta/dr = 0$, as soon as $t \geq 40$ (figures 13(c) and 14). According to the Rayleigh's
 602 inflectional criterion (Rayleigh 1880), this is a necessary condition for the shear instability.
 603 However, only the first extremum, where ζ has a local minimum, satisfies the stiffer Fjørtoft
 604 (1950) instability condition $[\Omega(r) - \Omega(r_I)]\partial\zeta/\partial r < 0$, where r_I is the extremum. This gives
 605 us hindsight on the possible origin of the late non-axisymmetric evolution of the vertical
 606 vorticity. The next section will investigate whether or not this hypothesis is correct.

607 6. Analysis of the non-axisymmetric evolution

608 As seen in the previous sections, a ring of anomalous vertical vorticity develops near the
 609 critical radius and, subsequently, this ring may become non-axisymmetric when the non-
 610 traditional Rossby number \widetilde{Ro} is below a critical value depending on the Reynolds number
 611 (figure 8). In this section, the main question is: what is the origin of this non-axisymmetric
 612 evolution? Is it due to a shear instability associated to the inflection point in the vertical
 613 vorticity profile (see figure 14)? or is it an intrinsic behaviour of the vortex under the
 614 complete Coriolis force? Regarding the latter hypothesis, we have seen indeed from (4.27-
 615 4.29) that the vertical velocity field forces not only an axisymmetric vertical vorticity field
 616 but also a non-axisymmetric one with an azimuthal wavenumber $m = 2$.

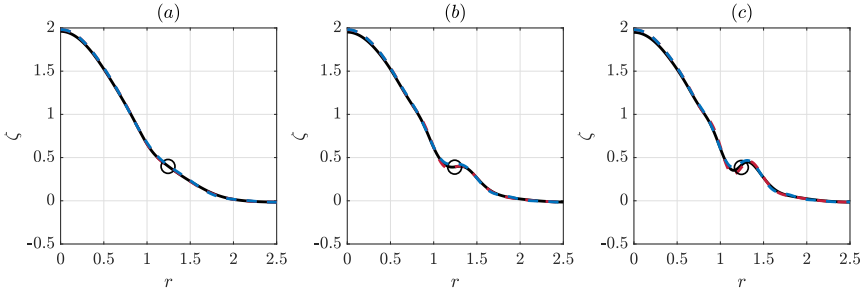


Figure 13: Comparison between the vertical vorticity at $\theta = \pi/2$ in the DNS (black solid line) and the asymptotic expressions $\zeta = \zeta_0 + \varepsilon^2 \zeta_{20}$ where ζ_{20} follows the unsteady inviscid solution (4.31) (red dashed line) and $\zeta = \zeta_0 + \zeta_1$ with ζ_1 given by the non-linear equations (4.45,4.47) (blue dashed line) at (a) $t = 25$, (b) $t = 35$ and (c) $t = 40$ for $Re = 10000$, $F_h = 2$, $Ro = 20.3$, $\phi = 80^\circ$ ($\bar{Ro} = 115.2$). The circle symbols represent the location of the critical radius in the unsteady inviscid solution (4.31).

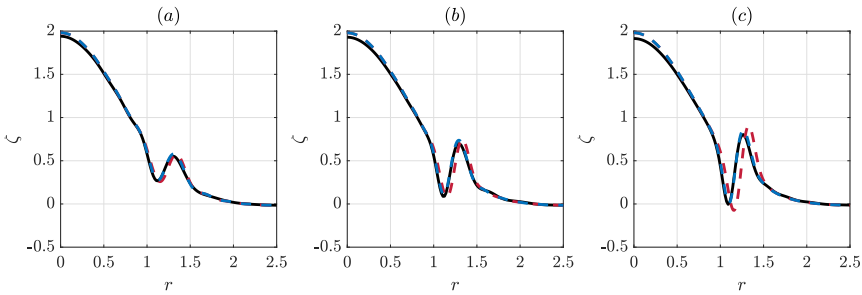


Figure 14: Comparison between the vertical vorticity at $\theta = \pi/2$ in the DNS (black solid line) and the asymptotic expressions $\zeta = \zeta_0 + \varepsilon^2 \zeta_{20}$ where ζ_{20} follows the unsteady viscous solution (4.35) (red dashed line) and $\zeta = \zeta_0 + \zeta_1$ with ζ_1 given by the non-linear equations (4.45,4.47) (blue dashed line) at (a) $t = 50$, (b) $t = 65$ and (c) $t = 85$ for $Re = 10000$, $F_h = 2$, $Ro = 20.3$, $\phi = 80^\circ$ ($\bar{Ro} = 115.2$). The circle symbols represent the location of the critical radius in the unsteady inviscid solution (4.35).

617

6.1. Azimuthal decomposition of ζ and u_z

618 In order to better understand the onset of non-axisymmetric vertical vorticity, we have first
619 decomposed ζ thanks to an azimuthal Fourier transform

$$620 \quad \hat{\zeta}_m(r, t) = \int_0^{2\pi} \zeta(r, \theta, t) e^{-im\theta} d\theta, \quad (6.1)$$

621 where $\zeta(x, y, t)$ has been first interpolated on a grid of cylindrical coordinates (r, θ) . The
622 same transform has been applied to u_z in order to obtain \hat{u}_{z_m} . The mean power in each
623 azimuthal wavenumber is then defined as

$$624 \quad E_\zeta(m, t) = \frac{\int_0^{l_x/2} \hat{\zeta}_m^2(r, t) r dr}{\int_0^{l_x/2} r dr} = \frac{8}{l_x^2} \int_0^{l_x/2} \hat{\zeta}_m^2(r, t) r dr, \quad (6.2)$$

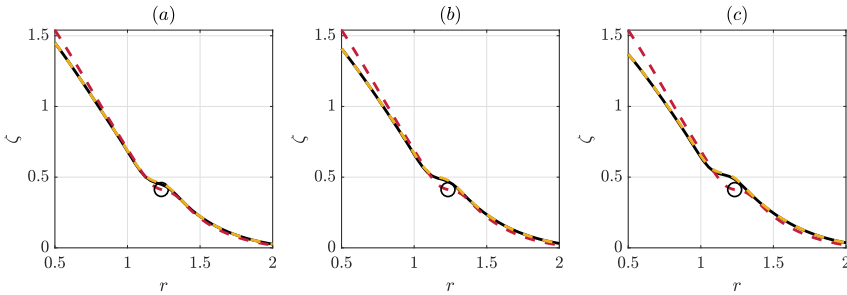


Figure 15: Comparison between the vertical vorticity at $\theta = \pi/2$ in the DNS (black solid line) and the asymptotic expressions $\zeta = \zeta_0 + \varepsilon^2 \zeta_{20}$ where ζ_{20} follows the viscous solution (4.36) (red dashed line) and $\zeta = \zeta_0 + \zeta_1$ with ζ_1 given by the non-linear equations (4.45,4.47) and the viscous decay of ζ_0 also taken into account (yellow dashed line) at (a) $t = 200$, (b) $t = 300$ and (c) $t = 400$ for $Re = 10000$, $F_h = 2$, $Ro = 20.0$, $\phi = 87.7^\circ$ ($\widetilde{Ro} = 500$). The circle symbols represent the location of the critical radius in the viscous solution (4.36).

625 and

$$626 \quad E_{u_z}(m, t) = \frac{8}{l_x^2} \int_0^{l_x/2} \hat{u}_{z_m}^2(r, t) r dr. \quad (6.3)$$

627 Figure 16(a) displays the evolution of the logarithm of the power of the first three azimuthal
 628 wavenumbers of the vertical vorticity. These are only even, i.e. $m = 0, m = 2, m = 4$. Similarly,
 629 figure 16(b) shows the logarithm of the power of the first three azimuthal wavenumbers of
 630 u_z . They are odd in this case: $m = 1, m = 3, m = 5$. It can be seen that $E_\zeta(0, t)$ and
 631 $E_{u_z}(1, t)$ (black solid lines) remain approximately constant except that $E_{u_z}(1, t)$ sustains
 632 large oscillation after $t \approx 120$.

633 It is also worth to point out that $E_\zeta(2, t)$ starts to grow at the beginning of the simulation
 634 since ζ_{22} increases like t^2 due to the forcing by the vertical velocity as shown in §4.3.1 (figure
 635 16 (b)). However, when $t \leq 80$, its power remains negligible compared to the one of the
 636 axisymmetric mode, $E_\zeta(0, t)$. In contrast, after $t \approx 80$, $E_\zeta(2, t)$ grows exponentially before
 637 saturating at $t \geq 120$. There is therefore a clear transition towards an exponential growth, a
 638 feature consistent with the instability hypothesis. Nevertheless, we can see that the azimuthal
 639 mode $m = 3$ of u_z (figure 16(b)) grows also exponentially at the same time. The higher
 640 modes, $m = 4$ of ζ and $m = 5$ of u_z , start to increase also exponentially but somewhat later.
 641 Thus, it is unclear if the growth of $E_{u_z}(3, t)$ is a consequence of the growth of $E_\zeta(2, t)$, if
 642 it is the opposite, or if the exponential growth is due to a coupling between $E_{u_z}(3, t)$ and
 643 $E_\zeta(2, t)$.

644

6.2. Truncated model

645 To answer the latter question, we have derived a truncated model taking into account only the
 646 first azimuthal wavenumbers of each quantity. More precisely, the different variables have
 647 been written as

$$648 \quad u_r = \hat{u}_{r_{2c}}(r, t) \cos(2\theta) + \hat{u}_{r_{2s}}(r, t) \sin(2\theta), \quad (6.4a)$$

$$650 \quad u_\theta = \hat{u}_{\theta_0}(r, t) + \hat{u}_{\theta_{2c}}(r, t) \cos(2\theta) + \hat{u}_{\theta_{2s}}(r, t) \sin(2\theta), \quad (6.4b)$$

$$652 \quad p(r, \theta) = \hat{p}_0(r, t) + \hat{p}_{2c}(r, t) \cos(2\theta) + \hat{p}_{2s}(r, t) \sin(2\theta), \quad (6.4c)$$

$$654 \quad \zeta = \hat{\zeta}_0(r, t) + \hat{\zeta}_{2c}(r, t) \cos(2\theta) + \hat{\zeta}_{2s}(r, t) \sin(2\theta), \quad (6.4d)$$

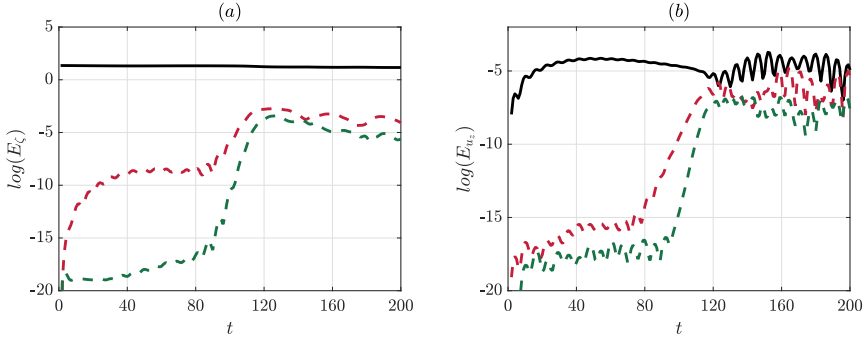


Figure 16: Evolution of the power (a) $E_\chi(m, t)$ for the azimuthal wavenumbers $m = 0$ (black solid line), $m = 2$ (red dashed line) and $m = 4$ (green dashed line) and the power (b) $E_{u_z}(m, t)$ for the azimuthal wavenumbers $m = 1$ (black solid line), $m = 3$ (red dashed line) and $m = 5$ (green dashed line) for $Re = 10000$, $F_h = 2$, $Ro = 20.3$ and $\phi = 80^\circ$ ($\widetilde{Ro} = 115.2$).

$$655 \quad u_z = \hat{u}_{z_{1c}}(r, t) \cos(\theta) + \hat{u}_{z_{1s}}(r, t) \sin(\theta), \quad (6.4e)$$

656

$$657 \quad b = \hat{b}_{1c}(r, t) \cos(\theta) + \hat{b}_{1s}(r, t) \sin(\theta). \quad (6.4f)$$

658 These decompositions have been introduced in (4.1a-4.1e) and the following governing
 659 equations have been obtained for the vertical velocity and buoyancy by truncating all the
 664 higher modes:

$$665 \quad \frac{\partial \hat{u}_{z_{1c}}}{\partial t} = -\frac{1}{2} \left(\hat{u}_{r_{2c}} \frac{\partial \hat{u}_{z_{1c}}}{\partial r} + \hat{u}_{r_{2s}} \frac{\partial \hat{u}_{z_{1s}}}{\partial r} \right) - \frac{1}{r} \left(\hat{u}_{\theta_0} \hat{u}_{z_{1s}} + \frac{1}{2} (\hat{u}_{\theta_{2c}} \hat{u}_{z_{1s}} - \hat{u}_{\theta_{2s}} \hat{u}_{z_{1c}}) \right) \\ + \hat{b}_{1c} + \frac{1}{Re} \nabla^2 \hat{u}_{z_{1c}} + \frac{1}{Ro} (\hat{u}_{r_{2c}} - \hat{u}_{\theta_{2s}}), \quad (6.5a)$$

$$666 \quad \frac{\partial \hat{u}_{z_{1s}}}{\partial t} = \frac{1}{2} \left(\hat{u}_{r_{2c}} \frac{\partial \hat{u}_{z_{1s}}}{\partial r} - \hat{u}_{r_{2s}} \frac{\partial \hat{u}_{z_{1c}}}{\partial r} \right) + \frac{1}{r} \left(\hat{u}_{\theta_0} \hat{u}_{z_{1c}} - \frac{1}{2} (\hat{u}_{\theta_{2c}} \hat{u}_{z_{1c}} + \hat{u}_{\theta_{2s}} \hat{u}_{z_{1s}}) \right) \\ + \hat{b}_{1s} + \frac{1}{Re} \nabla^2 \hat{u}_{z_{1s}} + \frac{1}{Ro} (\hat{u}_{r_{2s}} + \hat{u}_{\theta_{2c}} - 2\hat{u}_{\theta_0}), \quad (6.5b)$$

$$667 \quad \frac{\partial \hat{b}_{1c}}{\partial t} = -\frac{1}{2} \left(\hat{u}_{r_{2c}} \frac{\partial \hat{b}_{1c}}{\partial r} + \hat{u}_{r_{2s}} \frac{\partial \hat{b}_{1s}}{\partial r} \right) - \frac{1}{r} \left(\hat{u}_{\theta_0} \hat{b}_{1s} + \frac{1}{2} (\hat{u}_{\theta_{2c}} \hat{b}_{1s} - \hat{u}_{\theta_{2s}} \hat{b}_{1c}) \right) \\ - \frac{\hat{u}_{z_{1c}}}{F_h^2} + \frac{1}{ReSc} \nabla^2 \hat{b}_{1c}, \quad (6.5c)$$

$$668 \quad \frac{\partial \hat{b}_{1s}}{\partial t} = \frac{1}{2} \left(\hat{u}_{r_{2c}} \frac{\partial \hat{b}_{1s}}{\partial r} - \hat{u}_{r_{2s}} \frac{\partial \hat{b}_{1c}}{\partial r} \right) + \frac{1}{r} \left(\hat{u}_{\theta_0} \hat{b}_{1c} - \frac{1}{2} (\hat{u}_{\theta_{2c}} \hat{b}_{1c} + \hat{u}_{\theta_{2s}} \hat{b}_{1s}) \right) \\ - \frac{\hat{u}_{z_{1s}}}{F_h^2} + \frac{1}{ReSc} \nabla^2 \hat{b}_{1s}. \quad (6.5d)$$

669

673 Applying the same truncation approach for the vertical vorticity gives

$$674 \quad \frac{\partial \hat{\zeta}_0}{\partial t} = -\frac{1}{2} \left(\hat{u}_{r_{2c}} \frac{\partial \hat{\zeta}_{2c}}{\partial r} + \hat{u}_{r_{2s}} \frac{\partial \hat{\zeta}_{2s}}{\partial r} \right) - \frac{1}{r} (\hat{u}_{\theta_{2c}} \hat{\zeta}_{2s} - \hat{u}_{\theta_{2s}} \hat{\zeta}_{2c}) + \frac{1}{Re} \nabla^2 \hat{\zeta}_0, \quad (6.6a)$$

$$+ \frac{1}{Ro} \left(\frac{\partial \hat{u}_{z_{1s}}}{\partial r} + \frac{\hat{u}_{z_{1s}}}{r} \right)$$

$$675 \quad \frac{\partial \hat{\zeta}_{2c}}{\partial t} = -\hat{u}_{r_{2c}} \frac{\partial \hat{\zeta}_0}{\partial r} - \frac{2\hat{u}_{\theta_0}}{r} \hat{\zeta}_{2s} + \frac{1}{Re} \nabla^2 \hat{\zeta}_{2c} - \frac{1}{Ro} \left(\frac{\partial \hat{u}_{z_{1s}}}{\partial r} - \frac{\hat{u}_{z_{1s}}}{r} \right), \quad (6.6b)$$

$$676 \quad \frac{\partial \hat{\zeta}_{2s}}{\partial t} = -\hat{u}_{r_{2s}} \frac{\partial \hat{\zeta}_0}{\partial r} + \frac{2\hat{u}_{\theta_0}}{r} \hat{\zeta}_{2c} + \frac{1}{Re} \nabla^2 + \frac{1}{Ro} \left(\frac{\partial \hat{u}_{z_{1c}}}{\partial r} - \frac{\hat{u}_{z_{1c}}}{r} \right), \quad (6.6c)$$

678 where

$$679 \quad \hat{\zeta}_0 = \frac{1}{r} \frac{\partial r \hat{u}_{\theta_0}}{\partial r}, \quad (6.7a)$$

$$681 \quad \hat{\zeta}_{2c} = \frac{1}{r} \frac{\partial r \hat{u}_{\theta_{2c}}}{\partial r} - \frac{2}{r} \hat{u}_{r_{2s}}, \quad (6.7b)$$

$$683 \quad \hat{\zeta}_{2s} = \frac{1}{r} \frac{\partial r \hat{u}_{\theta_{2s}}}{\partial r} + \frac{2}{r} \hat{u}_{r_{2c}}. \quad (6.7c)$$

684 The divergence equation also implies

$$685 \quad \frac{1}{r} \frac{\partial r \hat{u}_{r_{2c}}}{\partial r} + \frac{2}{r} \hat{u}_{\theta_{2s}} = 0, \quad (6.8a)$$

$$687 \quad \frac{1}{r} \frac{\partial r \hat{u}_{r_{2s}}}{\partial r} - \frac{2}{r} \hat{u}_{\theta_{2c}} = 0. \quad (6.8b)$$

688 Such truncated model can be seen as a heuristic extension of the asymptotic analyses.
 689 Indeed, it takes into account both time dependence and diffusive effects in the evolution of
 690 the vertical velocity and buoyancy (6.5). Moreover, the modifications of the axisymmetric
 691 flow field (\hat{u}_{θ_0}) and the generated $m = 2$ mode ($\hat{u}_{r_{2c}}$, $\hat{u}_{r_{2s}}$, $\hat{u}_{\theta_{2c}}$, $\hat{u}_{\theta_{2s}}$) are also taken into
 692 account. The latter is governed by (6.6b-6.6c) and it appears also in the evolution of the
 693 axisymmetric flow field (6.6a). However, like in the asymptotic analyses, only the first
 694 azimuthal wavenumber of u_z and b are considered, i.e. the mode $m = 3$, $m = 5$, ... are
 695 neglected. Similarly, the higher modes $m = 4$, $m = 6$, ... are neglected in the evolution of the
 696 horizontal flow field (6.6).

697 Figures 17 (a, b) compares the power $E_{\zeta}(2, t)$ and $E_{u_z}(1, t)$, respectively, obtained in the
 698 DNS and in the truncated model. There are some differences for $t \geq 100$ but, qualitatively,
 699 the same type of evolution as in the DNS is obtained with the truncated model. This is remarkable
 700 since the truncated model crudely neglects many azimuthal modes and, in particular, the
 701 azimuthal mode $m = 3$ in the vertical velocity and buoyancy fields. Hence, this proves
 702 that the growth of $E_{u_z}(3, t)$ in figure 16(b) does not play a key role in the onset of non-
 703 axisymmetry in the vertical vorticity.

704 We can make a step further in the understanding of this phenomenon by freezing the
 705 axisymmetric velocity field. In other words, the time evolution of $(\hat{u}_{\theta_0}, \hat{\zeta}_0)$ is suppressed
 706 after a given time t_f . We also set the forcing terms due to the non-traditional Coriolis force
 707 to be zero in (6.6b) and (6.6c). Hence, the latter equations become

$$708 \quad \frac{\partial \hat{\zeta}_{2c}}{\partial t} = -\hat{u}_{r_{2c}} \frac{\partial \hat{\zeta}_0(r, t_f)}{\partial r} - \frac{2\hat{u}_{\theta_0}(r, t_f)}{r} \hat{\zeta}_{2s} + \frac{1}{Re} \nabla^2 \hat{\zeta}_{2c}, \quad (6.9a)$$

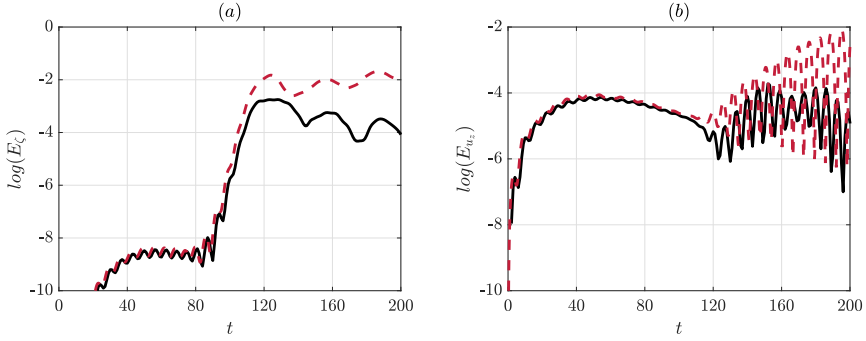


Figure 17: Evolution of the power (a) $E_\zeta(2, t)$ and (b) $E_{u_z}(1, t)$ in the DNS (black solid line) and in the truncated model (red dashed line) for $Re = 10000$, $F_h = 2$, $Ro = 20.3$ and $\phi = 80^\circ$ ($\widetilde{Ro} = 115.2$).

$$709 \quad \frac{\partial \hat{\zeta}_{2s}}{\partial t} = -\hat{u}_{r_{2s}} \frac{\partial \hat{\zeta}_0(r, t_f)}{\partial r} + \frac{2\hat{u}_{\theta_0}(r, t_f)}{r} \hat{\zeta}_{2c} + \frac{1}{Re} \nabla^2 \hat{\zeta}_{2s}. \quad (6.9b)$$

710 These equations describe simply the linear evolution of perturbations with azimuthal
 711 wavenumber $m = 2$ on a steady axisymmetric vortex with azimuthal velocity $\hat{u}_{\theta_0}(r, t_f)$. The
 712 perturbations $(\hat{u}_{r_{2c}}, \hat{u}_{\theta_{2c}})$ and $(\hat{u}_{r_{2s}}, \hat{u}_{\theta_{2s}})$ are initialized by a white noise whose amplitude is
 713 adjusted so as to have a power of the same order as $E_\zeta(2, t_f)$. Figure 18 shows the evolution
 714 of the power $E_\zeta(2, t)$ for different freezing time t_f ; $t_f = 40$ (yellow dashed line), $t_f = 50$
 715 (blue dashed line), $t_f = 65$ (red dashed line), $t_f = 85$ (green dashed line) compared to the
 716 evolution of $E_\zeta(2, t)$ in the truncated model (black solid line). Strikingly, we see that $E_\zeta(2, t)$
 717 grows also exponentially regardless of the value of t_f investigated. Furthermore, the growth
 718 rate, i.e. the slope, increases with t_f . Most interestingly, the growth rate for $t_f = 85$ is close to
 719 the one observed in the truncated model (black solid line). This demonstrates that the onset
 720 of non-axisymmetry in the vertical vorticity is due to an instability of the vortex profile.
 721 When the anomaly of vertical vorticity is sufficient to have an extremum, a shear instability
 722 with an azimuthal wavenumber $m = 2$ develops. Subsequently, this triggers the growth of
 723 higher azimuthal modes through the coupling with the non-traditional Coriolis force.

724 6.3. Equivalent vortex with piecewise uniform vorticity

725 A simple model of the instability can be obtained by considering the inviscid limit and by
 726 using a vortex with piecewise uniform vorticity with four concentric regions as considered
 727 by Carton & Legras (1994) and Kossin *et al.* (2000). As shown by two examples in figure
 728 19, the vorticity profile in the DNS can be crudely approximated by four levels of constant
 729 vorticity:

$$730 \quad \zeta = \begin{cases} \zeta_1 = 2 & 0 < r < r_1 \\ \zeta_2 = \zeta_c - \delta_v/2 & r_1 < r < r_2 \\ \zeta_3 = \zeta_c + \delta_v/2 & r_2 < r < r_3 \\ \zeta_4 = 0 & r_3 < r \end{cases} \quad (6.10)$$

731 where $r_1 = r_c - \delta_h$, $r_2 = r_c$ and $r_3 = r_c + \delta_h$ where δ_v and δ_h are the amplitude and size
 732 of the vorticity anomaly in the vicinity of the critical radius r_c . More explicitly, δ_v is the
 733 difference between the local maximum and minimum of the vorticity and δ_h is the distance
 734 between these two extrema. The corresponding angular velocity of the vortex is continuous

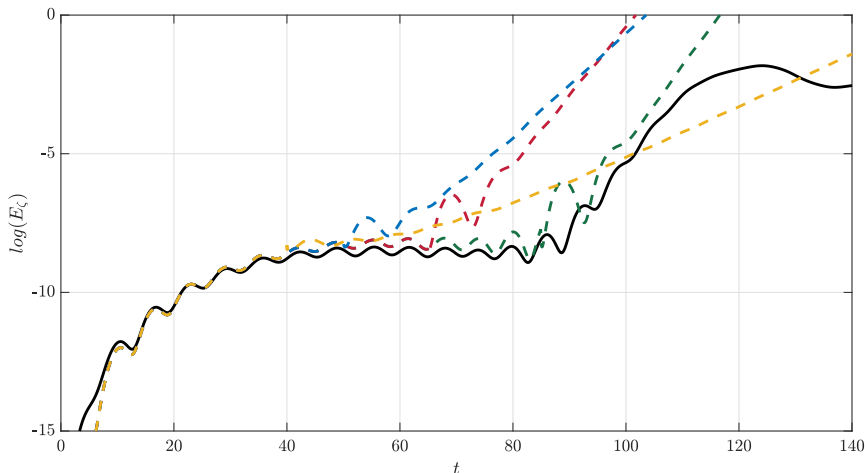


Figure 18: Evolution of the power $E_\zeta(2, t)$ in the truncated model (black solid line) or using (6.9) for different freezing times: $t_f = 85$ (green dashed line), $t_f = 65$ (red dashed line), $t_f = 50$ (blue dashed line) and $t_f = 40$ (yellow dashed line) for $\widetilde{Re} = 10000$, $F_h = 2$, $Ro = 20.3$ and $\phi = 80^\circ$ ($\widetilde{Ro} = 115.2$).

735 and given by

$$736 \quad \Omega(r) = \frac{1}{2} \begin{cases} \zeta_1 & 0 < r < r_1 \\ \zeta_2 - (\zeta_2 - \zeta_1)(r_1/r)^2 & r_1 < r < r_2 \\ \zeta_3 - (\zeta_2 - \zeta_1)(r_1/r)^2 - (\zeta_3 - \zeta_2)(r_2/r)^2 & r_2 < r < r_3 \\ -(\zeta_2 - \zeta_1)(r_1/r)^2 - (\zeta_3 - \zeta_2)(r_2/r)^2 + \zeta_3(r_3/r)^2 & r_3 < r \end{cases} \quad (6.11)$$

737 For a given Froude number F_h , the position of the critical radius r_c and the value of ζ_c are
 738 fixed. Hence, the problem has only two control parameters: δ_v and δ_h . The stability of such
 739 vortex with respect to perturbations of the form $\psi e^{im\theta + \sigma t}$ is governed by the eigenvalue
 740 problem (Carton & Legras 1994; Kossin *et al.* 2000)

$$741 \quad \begin{pmatrix} m\Omega(r_1) + \frac{1}{2}(\zeta_2 - \zeta_1) & \frac{1}{2}(\zeta_2 - \zeta_1)(r_1/r_2)^m & \frac{1}{2}(\zeta_2 - \zeta_1)(r_1/r_3)^m \\ \frac{1}{2}(\zeta_3 - \zeta_2)(r_1/r_2)^m & m\Omega(r_2) + \frac{1}{2}(\zeta_3 - \zeta_2) & \frac{1}{2}(\zeta_3 - \zeta_2)(r_2/r_3)^m \\ -\frac{1}{2}\zeta_3(r_1/r_3)^m & -\frac{1}{2}\zeta_3(r_2/r_3)^m & m\Omega(r_3) - \frac{1}{2}\zeta_3 \end{pmatrix} \begin{pmatrix} \psi_1 \\ \psi_2 \\ \psi_3 \end{pmatrix} = \sigma \begin{pmatrix} \psi_1 \\ \psi_2 \\ \psi_3 \end{pmatrix}. \quad (6.12)$$

742 Figure 20 (a) shows the growth rate contours for the $m = 2$ perturbations for $F_h = 2$
 743 as a function of (δ_v, δ_h) . We see that the growth rate is positive only when δ_v and δ_h are
 744 sufficiently away from zero in the ranges investigated. The symbols in figure 20(a) indicate
 745 the parameters (δ_v, δ_h) estimated by fitting (6.10) to the vorticity field $\zeta_0(r, t_f)$ at different
 746 times t_f for $F_h = 2$, for two different latitudes $\phi = 80^\circ$ (red circles) and $\phi = 75^\circ$ (black
 747 squares). For example, for $\phi = 80^\circ$, the time t_f varies from $t_f = 45$ (leftmost point) to $t_f = 85$
 748 (rightmost point). The size of the vorticity anomaly δ_h does not vary very much and is around
 749 $\delta_h \simeq 0.2$ for both latitudes. In contrast, the amplitude of the anomaly δ_v increases with t_f
 750 as expected. Figure 20(b) displays the growth rate as a function of δ_v (circle and square
 751 symbols). The dashed lines show the corresponding growth rate computed from (6.9), i.e. by
 752 considering the continuous vorticity profile $\zeta_0(r, t_f)$ and with the perturbations initialized
 753 by white noise. This shows that the piecewise vortex model is able to predict quite well

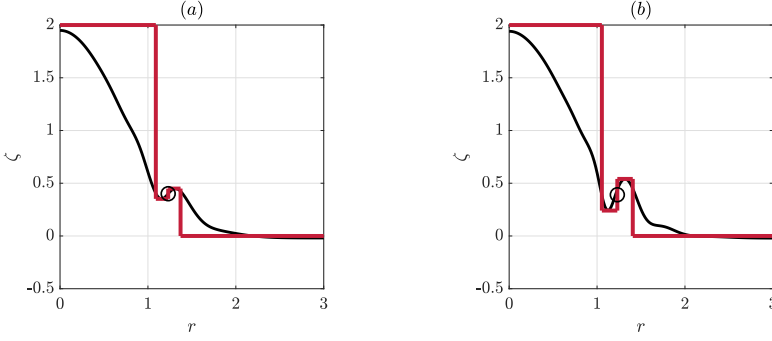


Figure 19: Examples of the piecewise uniform vorticity (red line) fitting the continuous vertical vorticity profiles (black line) at (a) $t = 40$, (b) $t = 50$ for $Re = 10000$, $F_h = 2$, $Ro = 20.3$ and $\phi = 80^\circ$ ($\widetilde{Ro} = 115.2$). The circle symbols represent the location of the critical radius.

754 the growth rate of the instability observed in the truncated model, which is itself in good
755 agreement with the DNS.

756 Using (6.12), we have also computed the growth rate of higher azimuthal wavenumbers
757 $m > 2$. The results show that the most unstable wavenumber is not $m = 2$ but is between
758 $m = 3$ and $m = 5$ for the parameters indicated by the symbols in figure 20(a). Three reasons
759 might explain the actual dominance of $m = 2$. First, the velocity jumps in the piecewise
760 vortex model could favor larger wavenumbers compared to a continuous vorticity profile.
761 Second, we have seen from (4.27-4.28) that the non-traditional Coriolis force generates
762 not only an axisymmetric vorticity at order $1/\widetilde{Ro}^2$ but also a vorticity field with with an
763 azimuthal wavenumber $m = 2$. Figure 17(a) shows that the latter is weak before the onset
764 of the instability. However, it is not zero and, therefore, this small amplitude could favor
765 its dominance over more unstable higher wavenumbers whose initial amplitudes are much
766 lower (see $m = 4$ in figure 17(a)). Third, the vortex profile is continuously evolving with
767 time while, in the stability problems (6.9) or (6.12), we have frozen this evolution. Hence,
768 the $m = 2$ wavenumber could be selected first when the vortex becomes slightly unstable.
769 This early selection would then ensure its subsequent dominance even if it is no longer the
770 most unstable wavenumber. Such effect has been evidenced by Wang & Balmforth (2021) in
771 their study of the evolution of the wavenumber selection as the critical layer becomes finer.

772

6.4. Theoretical criterion

773 Even if the Rayleigh-Fjørtoft criterion is only a necessary condition for the shear instability
774 in inviscid fluids, we can try to use it to establish a theoretical criterion for the onset of the
775 shear instability in the DNS for finite Reynolds numbers. Since the radial derivative of the
776 vorticity is maximum at $r = r_c$ and is negative away from the critical radius, a necessary
777 condition ensuring that there exists extrema, $d\zeta/dr = 0$, reads

$$778 \quad \frac{d\zeta(r_c, t_s)}{dr} \geq c, \quad (6.13)$$

779 where $c = 0$ is the minimum requirement for the existence of an inflection point, but we
780 have explored also the consequences of larger values of c . Besides, the time t_s will be set
781 as $t_s = a\mathcal{T}$, where a is a constant larger than unity. Indeed, the onset of the shear instability
782 always occurs after the time \mathcal{T} . Therefore, the vorticity ζ will be taken as the asymptotic
783 axisymmetric vorticity $\zeta = \zeta_0 + \varepsilon^2 \zeta_{20}$ where ζ_{20} is given by (4.36). As seen in figure 12,

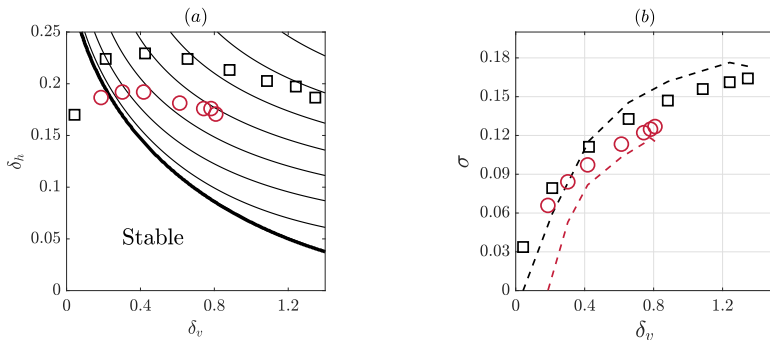


Figure 20:

(a) Growth rates contours of the piecewise vortex model as a function of δ_h and δ_v for $F_h = 2$. The contour interval is 0.03. The bold line indicates the growth rate $\sigma = 0$. The symbols correspond to the values of δ_h and δ_v estimated at different freezing times for $\phi = 80^\circ$ ($\widetilde{Ro} = 115.2$) (red circles) and $\phi = 75^\circ$ ($\widetilde{Ro} = 77.27$) (black squares) for $Re = 10000$, $F_h = 2$.

(b) Growth rates as a function of δ_v obtained by the truncated model at different freezing times (symbols) and given by (6.12) for $m = 2$ (dashed lines) for $\phi = 75^\circ$ ($\widetilde{Ro} = 77.27$) (black) and $\phi = 80^\circ$ ($\widetilde{Ro} = 115.2$) (red), $Re = 10000$ and $F_h = 2$.

784 $\partial\zeta_{20}/\partial r(r_c, t)$ is indeed well predicted by (4.36) for large times. Then, (6.13) becomes

$$785 \quad \frac{Re^{2/3}}{\widetilde{Ro}} \geq \left| 2\Omega'_c \right|^{1/3} \left(1 + \frac{1}{Sc} \right)^{1/6} \sqrt{\frac{c - 3\Omega'_c - r_c \Omega''_c}{2\pi r_c \Omega_c \left(\text{Hi}(0) - \left(\frac{1 + 1/Sc}{8a\pi^2 \text{Hi}(0)} \right)^{1/2} \right)}}. \quad (6.14)$$

786 Remarkably, the right-hand side depends only on the Froude number through r_c , the Schmidt
 787 number Sc and the constants a and c . The criterion (6.14) when $c = 0$ and $a = \infty$ is represented
 788 by a solid line in figure 8. It delimits quite well the quasi-axisymmetric/non-axisymmetric
 789 domains observed in the DNS, except for the lowest Reynolds number investigated $Re = 2000$.
 790 Such difference for moderate Reynolds and Rossby numbers is not surprising since the
 791 asymptotics have been derived for high Reynolds number and large Rossby number \widetilde{Ro} .
 792 Furthermore, viscous effects might damp the shear instability growth when the Reynolds
 793 number is moderate.

794 As seen from the piecewise vortex model, the shear instability for $m = 2$ does not appear
 795 when $\delta_h \simeq 0.2$ as soon as $\delta_v > 0$. It can be roughly estimated that the instability arises
 796 only when δ_v such that $\delta_v/\delta_h \gtrsim 0.4$ (figure 20(a)). Therefore, we can estimate $\partial\zeta/\partial r =$
 797 $c \simeq \delta_v/\delta_h = 0.4$. The criterion (6.14) with this value of c and $a = \infty$ is represented by a
 798 dashed line in figure 8. The agreement with the DNS is as good as the criterion (6.14) with
 799 $c = 0$. The actual threshold is likely to be in between these two curves, i.e. in the hatched
 800 region (figure 8). Finally, we stress that the criterion (6.14) applies only to the shear instability
 801 due to an inflection point and not to other types of instability that may exist in viscous shear
 802 flows.

803 7. Late evolution of the vortex

804 Finally, figures 21 and 22 show the late evolution of the angular velocity profile (bottom row)
 805 when the instability develops or not, respectively. The DNS are the same as those already
 806 presented in section §3 for $Re = 2000$, $F_h = 2$ and different latitudes: $\phi = 60^\circ$ ($\widetilde{Ro} = 40$)

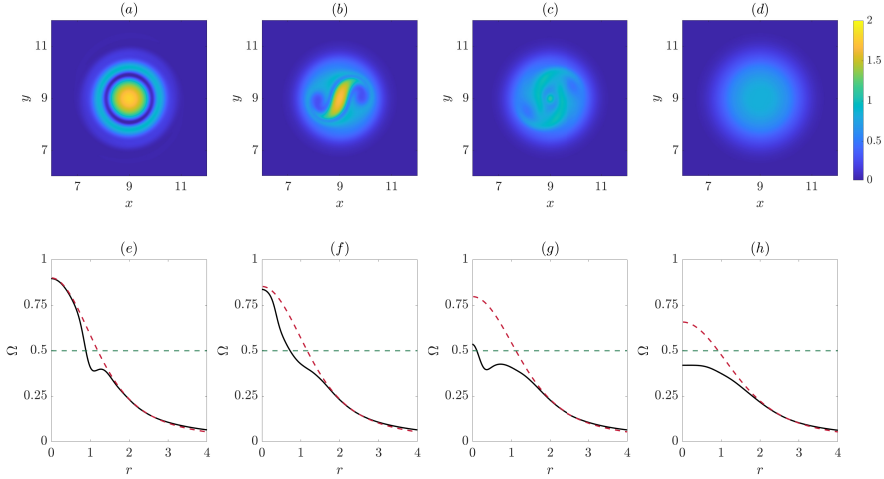


Figure 21: Vertical vorticity (top) and angular velocity profile (bottom) obtained from DNS (black line) at (a, e) $t = 50$, (b, f) $t = 80$, (c, g) $t = 120$ and (d, h) $t = 250$ for $Re = 2000$, $F_h = 2$, $Ro = 23.1$, $\phi = 60^\circ$ ($\widetilde{Ro} = 40$). The red dashed lines show the angular velocity profile if only viscous diffusion were active. The horizontal green dashed line represents the critical angular velocity value $1/F_h$.

807 (figures 4 and 21) and $\phi = 80^\circ$ ($\widetilde{Ro} = 115.2$) (figures 6 and 22). The corresponding
808 vorticity fields are also shown again in the top row of figures 21 and 22 for convenience. In
809 figures 21(c, d, g, h), we see that the instability ceases when the angular velocity is almost
810 everywhere below $1/F_h$ (horizontal green dashed line), i.e. when a critical radius no longer
811 exists. Due to the development of the critical layer and resulting instability, the decay of
812 the angular velocity in the vortex core is accelerated compared to a pure viscous decay
813 $\Omega = \frac{1}{r^2}(1 - \exp(\frac{-r^2}{1+4t/Re}))$ (shown by red dashed lines in figures 21(e, f, g, h)). When there
814 is no instability (figure 22), the evolution of the angular velocity is slower and follows more
815 closely a pure viscous diffusion law except in the vicinity of the critical radius where the
816 decay is also slightly enhanced.

817 8. Conclusion

818 We have studied numerically and theoretically the evolution of a Lamb-Oseen vortex in a
819 stratified-rotating fluid under the complete Coriolis force on the f -plane. The problem is
820 governed mainly by the Froude number F_h , the Reynolds number Re and the non-traditional
821 Rossby number \widetilde{Ro} based on the horizontal component of the background rotation.

822 Starting from a purely two-dimensional axisymmetric vortex, the DNS shows that a strong
823 vertical velocity field with an azimuthal wavenumber $m = 1$ is generated at a particular radius
824 when the Froude number is larger than unity. This radius increases with the Froude number.
825 Simultaneously, the vertical vorticity develops a quasi-axisymmetric anomaly near the same
826 radius. Later, this anomalous ring may become fully non-axisymmetric with an azimuthal
827 wavenumber $m = 2$ when the Reynolds number is sufficiently large and the non-traditional
828 Rossby number \widetilde{Ro} not too large. At late time, the vorticity returns to a quasi-axisymmetric
829 shape. Even if the vertical velocity is non-zero, all the fields remain independent of the
830 vertical coordinate. In other words, the flow is 2D3C, i.e. two dimensional but with 3

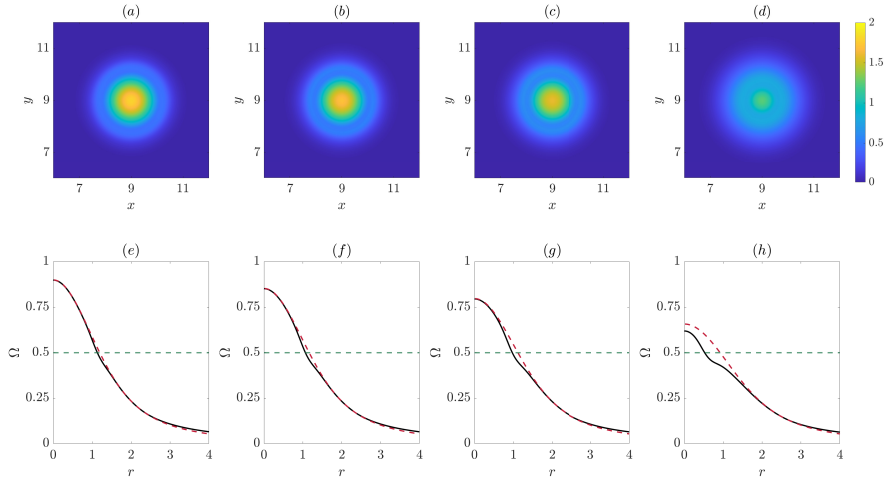


Figure 22: Vertical vorticity (top) and angular velocity profile (bottom) obtained from DNS (black line) at (a, e) $t = 50$, (b, f) $t = 80$, (c, g) $t = 120$ and (d, h) $t = 250$ for $Re = 2000$, $F_h = 2$, $Ro = 23.1$, $\phi = 80^\circ$ ($\widetilde{Ro} = 115.2$). The red dashed lines show the angular velocity profile if only viscous diffusion were active. The horizontal green dashed line represents the critical angular velocity value $1/F_h$.

831 velocity components. For this reason, the dynamics is independent of the traditional Rossby
 832 number Ro based on the vertical component of the background rotation.

833 An asymptotic analysis for large non-traditional Rossby number \widetilde{Ro} has allowed us to
 834 unravel this evolution. First, it shows that the non-traditional Coriolis force generates a
 835 vertical velocity and buoyancy fields at order $1/\widetilde{Ro}$ which are invariant along the vertical.
 836 When the Froude number F_h is larger than unity and in the absence of time dependence
 837 and viscous effects, these fields present a singularity at the radius where the angular velocity
 838 is equal to the Brunt–Väisälä frequency (i.e. the inverse of the Froude number in non-
 839 dimensional form). The asymptotic analyses show that this singularity is first regularized by
 840 the time dependence. This leads to a linear increase of the amplitude of the vertical velocity
 841 while the width of the critical layer shrinks at a rate inversely proportional to time. After a
 842 certain time, viscous effects saturate this evolution. The vertical velocity field is then steady
 843 with an amplitude proportional to $Re^{1/3}$ and a critical layer width scaling like $Re^{-1/3}$ as
 844 found by Boulanger *et al.* (2007) in the case of a tilted vortex in a stratified fluid. These
 845 asymptotic predictions are all in very good agreement with the DNS.

846 In turn, the non-traditional Coriolis force due to the vertical velocity modifies the vertical
 847 vorticity field at order $1/\widetilde{Ro}^2$. The dominant effect is the development of an axisymmetric
 848 ring of anomalous vorticity near the critical radius. This leads to the development of extrema
 849 in the vorticity profile. Again, the asymptotic predictions for the axisymmetric component
 850 of the vorticity are in good agreement with the DNS. Following Wang & Balmforth (2020,
 851 2021), we have further carried out a non-linear asymptotic analysis that takes into account
 852 the effect of the anomaly of axisymmetric vorticity back on the evolution of the vertical
 853 velocity. The predictions of this non-linear analysis are in better agreement with the DNS
 854 than those of the linear analysis indicating that both viscous and nonlinear effects operate in
 855 the critical layer.

856 In order to understand the origin of the subsequent non-axisymmetric evolution of the

857 vorticity field, we have first decomposed the vertical velocity and vorticity in the DNS by
 858 an azimuthal Fourier transform. This analysis shows that several azimuthal modes grow
 859 exponentially during the onset of non-axisymmetry: the odd modes $m = 3, m = 5$, etc for the
 860 vertical velocity and the even modes $m = 2, m = 4$, etc for the vertical vorticity. We have then
 861 introduced a highly truncated model which keeps only the $m = 1$ azimuthal wavenumber of
 862 the vertical velocity and the $m = 0$ and $m = 2$ wavenumbers of the vertical vorticity. Such
 863 truncated model exhibits also an onset of non-axisymmetry like in the DNS demonstrating
 864 that this behavior is not due to an unstable coupling between azimuthal modes. Furthermore,
 865 we have shown that if we freeze the profile of the axisymmetric component of the vertical
 866 vorticity at the time where the non-axisymmetry starts to appear and initializes the $m = 2$
 867 mode by white noise, the latter mode grows exponentially at a rate comparable to the one
 868 observed in the DNS. In addition, the stability of an equivalent piecewise vortex model
 869 with four levels of vorticity has been investigated and have been found to give growth rates
 870 for $m = 2$ in agreement with those of the truncated model. Altogether, this proves that the
 871 onset of non-axisymmetry comes from a two-dimensional shear instability related to the
 872 presence of a minimum in the vorticity profile. Finally, using the asymptotic expression of
 873 the axisymmetric component of the vorticity at late time at leading orders, the necessary
 874 condition for the shear instability has been converted into an instability condition in terms of
 875 (Re, \widetilde{Ro}) . This condition delimits well the quasi-axisymmetric/non-axisymmetric domains
 876 in the parameter space (Re, \widetilde{Ro}) .

877 The overall effect of the instability is to accelerate the decay of the angular velocity
 878 compared to a pure viscous diffusion. The instability ceases when the angular velocity is
 879 everywhere lower than the Brunt–Väisälä frequency (i.e. the inverse of the Froude number
 880 in non-dimensional form).

881 In summary, we have seen that the dynamics of a vortex for large Reynolds number can
 882 be strongly affected by the non-traditional Coriolis force even if the non-traditional Rossby
 883 number \widetilde{Ro} is large, i.e. even for a small value of the horizontal component of the background
 884 rotation. Since the typical Reynolds number of geophysical vortices is generally huge, this
 885 means that the non-traditional Coriolis force might have much more impact than expected
 886 by just considering its order of magnitude through the non-traditional Rossby number \widetilde{Ro} .
 887 It should be reminded however that another crucial condition is $F_h > 1$ that ensures the
 888 presence of a critical layer. Hence, such process might affect intense but not too large
 889 vortices in geophysical flows.

890 In the future, we will investigate the effect of three-dimensional perturbations on this
 891 phenomenon. Indeed, the vertical velocity is also responsible for an axial shear that might
 892 lead to another kind of shear instability if small three-dimensional perturbations are present
 893 as observed by Boulanger *et al.* (2007) for the case of a tilted vortex. It could be interesting
 894 also to study the configurations where the vortex is initially aligned with the background
 895 rotation vector or not columnar.

896 **Acknowledgements.** We thank the referees for their helpful comments that have improved the manuscript.

897 **Funding.** This work was performed using HPC resources from GENCI-IDRIS (grant 2020-A0082A07419).

898 **Declaration of interests.** The authors report no conflict of interest.

899 **Appendix A. Approximation of the solution of (4.34) for large time**

900 The solution (4.35) can be simplified for large time $T \gg 1$, i.e. $t \gg Re^{1/3}$. It is first convenient
901 to derive ζ_{20} with respect to \tilde{r} .

$$902 \quad \frac{\partial \zeta_{20}}{\partial \tilde{r}} = \frac{ReA}{2\gamma\pi} \int_0^{|\Omega'_c|T} \exp\left(\frac{-q^3}{3\gamma^3} + iq\tilde{r}\right) \left(1 - \exp\left(q^3/|\Omega'_c| - q^2T\right)\right) dq + c.c. \quad (A 1)$$

903 By using the change of variable $z = q/\gamma$ for the first part of the integrand and $x = q\sqrt{T}$ for
904 the second part, (A 1) can be rewritten

$$905 \quad \frac{\partial \zeta_{20}}{\partial \tilde{r}} = \frac{ReA}{2\pi} \int_0^{|\Omega'_c|T/\gamma} \exp\left(\frac{-z^3}{3} + i\gamma z\tilde{r}\right) dz$$

$$906 \quad - \frac{ReA}{2\gamma\pi\sqrt{T}} \int_0^{|\Omega'_c|T^{3/2}} \exp\left(\frac{-x^3}{3\gamma^3T^{3/2}} + i\frac{x\tilde{r}}{\sqrt{T}} + \frac{x^3}{|\Omega'_c|T^{3/2}} - x^2\right) dx + c.c. \quad (A 2)$$

907 When $T \gg 1$, the first integral tends to the Scorer's function (Abramowitz & Stegun 1972)
908 whereas the terms proportional to $1/T^{3/2}$ can be neglected compared to the other terms in
909 the second integral. This yields

$$910 \quad \frac{\partial \zeta_{20}}{\partial \tilde{r}} \simeq \frac{ReA}{2} \text{Hi}(i\gamma\tilde{r}) - \frac{ReA}{2\gamma\pi\sqrt{T}} \int_0^{|\Omega'_c|T^{3/2}} \exp\left(-x^2 + i\frac{x\tilde{r}}{\sqrt{T}}\right) dx + c.c. \quad (A 3)$$

911 By introducing another change of variable

$$912 \quad U = x - \frac{i\tilde{r}}{2\sqrt{T}}, \quad (A 4)$$

913 (A 3) becomes

$$914 \quad \frac{\partial \zeta_{20}}{\partial \tilde{r}} \simeq \frac{ReA}{2} \text{Hi}(i\gamma\tilde{r}) - \frac{ReA}{2\gamma\pi\sqrt{T}} \exp\left(\frac{-\tilde{r}^2}{4T}\right) \int_{-i\tilde{r}/(2\sqrt{T})}^{|\Omega'_c|T^{3/2} - i\tilde{r}/(2\sqrt{T})} e^{-U^2} dU + c.c. \quad (A 5)$$

915 The imaginary terms in the integral cancel with those of the complex conjugate giving

$$916 \quad \frac{\partial \zeta_{20}}{\partial \tilde{r}} = \frac{ReA}{2} [\text{Hi}(i\gamma\tilde{r}) + \text{Hi}^*(i\gamma\tilde{r})] - \frac{ReA}{\gamma\pi\sqrt{T}} \exp\left(\frac{-\tilde{r}^2}{4T}\right) \int_0^{|\Omega'_c|T^{3/2}} e^{-U^2} dU. \quad (A 6)$$

917 The remaining integral can be approximated by $\sqrt{\pi}/2$ since $T \gg 1$, leading finally to

$$918 \quad \frac{\partial \zeta_{20}}{\partial \tilde{r}} = \frac{ReA}{2} [\text{Hi}(i\gamma\tilde{r}) + \text{Hi}^*(i\gamma\tilde{r})] - \frac{ReA}{2\gamma\sqrt{\pi T}} \exp\left(\frac{-\tilde{r}^2}{4T}\right). \quad (A 7)$$

919 Integrating back in \tilde{r} gives the approximation (4.37).

REFERENCES

- 920 ABRAMOWITZ, M. & STEGUN, I. A., ed. 1972 *Handbook of Mathematical Functions with Formulas, Graphs,*
921 *and Mathematical Tables*, tenth printing edn. Washington, DC, USA: U.S. Government Printing
922 Office.
- 923 BILLANT, P. & BONNICI, J. 2020 Evolution of a vortex in a strongly stratified shear flow. part 2. numerical
924 simulations. *J. Fluid Mech.* **893**, A18.

- 925 BONNICI, J. 2018 Vertical decorrelation of a vortex by an external shear flow in a strongly stratified fluid.
926 Phd thesis, Université Paris-Saclay.
- 927 BOULANGER, N., MEUNIER, P. & LE DIZES, S. 2007 Structure of a stratified tilted vortex. *J. Fluid Mech.* **583**,
928 443–458.
- 929 BOULANGER, N., MEUNIER, P. & LE DIZES, S. 2008 Tilt-induced instability of a stratified vortex. *J. Fluid*
930 *Mech.* **596**, 1–20.
- 931 CARTON, X. & LEGRAS, B. 1994 The life-cycle of tripoles in two-dimensional incompressible flows. *J. Fluid*
932 *Mech.* **267**, 53–82.
- 933 DELONCLE, A., BILLANT, P. & CHOMAZ, J. 2008 Nonlinear evolution of the zigzag instability in stratified
934 fluids: a shortcut on the route to dissipation. *J. Fluid Mech.* **599**, 229–239.
- 935 ETLING, D. 1971 The stability of an ekman boundary layer flow as influenced by thermal stratification. *Beitr.*
936 *Phys. Atmos.* **44**, 168–186.
- 937 FJØRTOFT, R. 1950 *Application of integral theorems in deriving criteria of stability for laminar flows and for*
938 *the baroclinic circular vortex*, vol. 17. Geophys. Publ.
- 939 GERKEMA, T., ZIMMERMAN, J.T.F., MAAS, L.R.M. & VAN HAREN, H. 2008 Geophysical and astrophysical
940 fluid dynamics beyond the traditional approximation. *Rev. Geophys.* **46** (2).
- 941 HAYASHI, M. & ITOH, H. 2012 The importance of the nontraditional coriolis terms in large-scale motions in
942 the tropics forced by prescribed cumulus heating. *J. Atmos. Sci.* **69** (9), 2699–2716.
- 943 IGEL, M.R. & BIELLO, J.A. 2020 The nontraditional coriolis terms and tropical convective clouds. *J. Atmos.*
944 *Sci.* **77** (12), 3985–3998.
- 945 KLOOSTERZIEL, R.C., CARNEVALE, G.F. & ORLANDI, P. 2017 Equatorial inertial instability with full coriolis
946 force. *J. Fluid Mech.* **825**, 69–108.
- 947 KOSSIN, J.P., SCHUBERT, W.H. & MONTGOMERY, M.T. 2000 Unstable interactions between a hurricane’s
948 primary eyewall and a secondary ring of enhanced vorticity. *J. Atmos. Sci.* **57** (24), 3893–3917.
- 949 PARK, J., PRAT, V., MATHIS, S. & BUGNET, L. 2021 Horizontal shear instabilities in rotating stellar radiation
950 zones-ii. effects of the full coriolis acceleration. *Astron. Astrophys.* **646**, A64.
- 951 RAYLEIGH, LORD 1880 On the stability, or instability, of certain fluid motions. *Proc. London Math. Soc.* **9**,
952 57–70.
- 953 SEMENOVA, I.P. & SLEZKIN, L.N. 2003 Dynamically equilibrium shape of intrusive vortex formations in the
954 ocean. *Fluid Dyn.* **38** (5), 663–669.
- 955 SHEREMET, V.A. 2004 Laboratory experiments with tilted convective plumes on a centrifuge: a finite angle
956 between the buoyancy force and the axis of rotation. *J. Fluid Mech.* **506**, 217–244.
- 957 TORT, M. & DUBOS, T. 2014 Dynamically consistent shallow-atmosphere equations with a complete coriolis
958 force. *Q. J. R. Meteorol. Soc.* **140** (684), 2388–2392.
- 959 TORT, M., DUBOS, T., BOUCHUT, F. & ZEITLIN, V. 2014 Consistent shallow-water equations on the rotating
960 sphere with complete coriolis force and topography. *J. Fluid Mech.* **748**, 789–821.
- 961 TORT, M., RIBSTEIN, B. & ZEITLIN, V. 2016 Symmetric and asymmetric inertial instability of zonal jets on
962 the-plane with complete coriolis force. *J. Fluid Mech.* **788**, 274–302.
- 963 WANG, C. & BALMFORTH, N.J. 2020 Nonlinear dynamics of forced baroclinic critical layers. *J. Fluid Mech.*
964 **883**.
- 965 WANG, C. & BALMFORTH, N. J. 2021 Nonlinear dynamics of forced baroclinic critical layers ii. *J. Fluid*
966 *Mech.* **917**, A48.
- 967 WIPPERMANN, F. 1969 The orientation of vortices due to instability of the ekman-boundary layer. *Beitr.*
968 *Phys. Atmos.* **42** (4), 225–244.
- 969 ZEITLIN, V. 2018 Symmetric instability drastically changes upon inclusion of the full coriolis force. *Phys.*
970 *Fluids* **30** (6), 061701.